

Anisotropic Statistics of Lagrangian Structure Functions and Helmholtz Decomposition

HAN WANG^{a,b} AND OLIVER BÜHLER^a

^aCenter for Atmosphere Ocean Science, Courant Institute of Mathematical Sciences, New York University,
New York City, New York

(Manuscript received 20 August 2020, in final form 2 February 2021)

ABSTRACT: We present a new method to estimate second-order horizontal velocity structure functions, as well as their Helmholtz decomposition into rotational and divergent components, from sparse data collected along Lagrangian observations. The novelty compared to existing methods is that we allow for anisotropic statistics in the velocity field and also in the collection of the Lagrangian data. Specifically, we assume only stationarity and spatial homogeneity of the data and that the cross covariance between the rotational and divergent flow components is either zero or a function of the separation distance only. No further assumptions are made and the anisotropy of the underlying flow components can be arbitrarily strong. We demonstrate our new method by testing it against synthetic data and applying it to the Lagrangian Submesoscale Experiment (LASER) dataset. We also identify an improved statistical angle-weighting technique that generally increases the accuracy of structure function estimations in the presence of anisotropy.

KEYWORDS: Sea/ocean surface; Ocean dynamics; Data processing; Kinematics; Tracers; Statistics; Trajectories

1. Introduction

Lagrangian observations have been playing a crucial role in the understandings of submesoscale dynamics (Richardson and Stommel 1948; Davis 1991; Poje et al. 2014; D'Asaro et al. 2018). Collected from flow-following devices such as buoys or surface drifters, with GPS tracking, they can resolve spatial scales well below the deformation radius of 10–50 km in the ocean, with temporal resolutions down to minutes (Özgökmen 2015; D'Asaro et al. 2017; Lumpkin et al. 2017). While maintaining the submesoscale-resolving accuracy, they could stay in the ocean for up to months and cover several degrees in latitude and longitude. Such a wide span in spatial and temporal scales provides the potential for resolving the transitions and interactions between submesoscale and mesoscale dynamics. As oceanic flows are usually turbulent, we will apply a statistical description, rather than a deterministic one. To describe the scale-dependent dynamics, second-order structure functions, which are convenient to estimate for irregularly sampled data and directly related to power spectra (LaCasce 2016; Callies et al. 2016) are often investigated from Lagrangian data (Poje et al. 2014, 2017; Beron-Vera and LaCasce 2016; Balwada et al. 2016; Essink et al. 2019; Pearson et al. 2019, 2020).


The Helmholtz decomposition of two-dimensional (2D) velocity $\mathbf{u} = u\mathbf{e}_x + v\mathbf{e}_y$, on a 2D flat plane (such as a patch of the

ocean surface on a tangent plane) separates the divergent and rotational components of the velocity via

$$u = -\psi_y + \phi_x, \quad v = \psi_x + \phi_y, \quad (1)$$

where ψ and ϕ are stream and potential functions, respectively. As quasigeostrophic flows are nearly nondivergent, a strongly divergent flow indicates the breaking of balance. The detection of balance breaking sheds light on classic open questions such as the dynamics underlying the double power law of the Nastrom and Gage (1985) kinetic energy spectrum (Bartello 1995; Bühler et al. 2014, hereafter BCF14; Lindborg 1999), and has also been of practical interests in recent studies of tracer dispersion (D'Asaro et al. 2018) and high-resolution altimetry data processing (Qiu et al. 2017; Cao et al. 2019). However, observational data often suffer from strong limitations. Ship track or aircraft track measurements are one dimensional (1D) only, satellite snapshots usually cannot resolve scales finer than 10 km and Lagrangian observations are sparse and potentially suffer from biased sampling (D'Asaro et al. 2018; Pearson et al. 2019, 2020).

Overcoming such limitations to untangle the balanced and unbalanced flows has been of great interest, and a decomposition method suitable for 1D spectra under the assumption of horizontal isotropy was developed by BCF14. Their method consists of two steps: first, a Helmholtz decomposition is developed for 1D spectral data. Second, if potential energy spectrum is also measured, an energy equipartition statement is used to separate the energy spectrum of linear inertia-gravity waves and of the geostrophic flow. Extensions and generalizations of the BCF14 method have since been actively developed. It was soon realized that the assumption of uncorrelatedness between ψ and ϕ is not necessary under isotropy for the Helmholtz decomposition (Callies et al. 2016); inclusions of nonhydrostratic effects by utilizing vertical velocity measurements are studied (Zhang et al. 2015; Callies et al. 2016); more recently, a quasigeostrophic component is added

 Supplemental information related to this paper is available at the Journals Online website: <https://doi.org/10.1175/JPO-D-20-0199.s1>.

^bCurrent affiliation: Department of Physics, University of Toronto, Toronto, Ontario, Canada.

Corresponding author: Han Wang, hannnwangus@gmail.com

to the diagnosis, allowing for weak nonlinearities in the decomposition algorithm (Wang and Bühler 2020; Waite 2020). The BCF14 Helmholtz decomposition formulae has also been adapted into second-order structure functions counterparts (Lindborg 2015), emerging as a practical Helmholtz decomposition algorithm in studies of Lagrangian observations (Balwada et al. 2016; Essink et al. 2019; Pearson et al. 2019).

All the Helmholtz decomposition algorithms mentioned above rely on the assumptions of temporal stationarity, spatial homogeneity and horizontal isotropy. In this work, while keeping stationarity and homogeneity, we attempt to relax isotropy in the treatments of Lagrangian observations. Anisotropy is of obvious relevance to atmospheric and oceanic flows, as angle-dependent flow features such as fronts and directional currents cannot exist without it. Some quantitative indicators of anisotropy include the eccentricity of the eddy covariance matrix (Hoskins et al. 1983; Stewart et al. 2015) and asymmetry in zonal and meridional dispersions (Beron-Vera and LaCasce 2016; LaCasce 2010), but to our knowledge these cannot be directly applied to diagnose anisotropic components in structure functions. Moreover, nonphysical values have been sometimes observed in the applications of the isotropic methods in both atmospheric and oceanic datasets (Lindborg 2015; Bühler et al. 2017, hereafter BKT17). Motivated by this, an anisotropic extension to the BCF14 method that applies to 1D power spectra is proposed in BKT17, which successfully suppresses some nonphysical values in the applications to ship track data taken at Gulf Stream.

The BKT17 method is developed specifically for treatments of 1D data, which inevitably suffers from some strong constraints on the forms of anisotropy. Lagrangian observations, albeit irregular and sparse, are not strictly restricted to a single spatial dimension as 1D ship tracks do, and in principle, could provide more angle-dependent information. In this work, we propose a new Helmholtz decomposition algorithm that is suitable for the sparse 2D measurements, which allows for a generic azimuthal Fourier expansion of 2D structure functions.

Another discovery made during our explorations is a new angle-weighted approach to estimate structure functions. To our knowledge, isotropic structure functions are commonly evaluated as unweighted ensemble averages within each separation distance bin. We show that even if one is only interested in the isotropic components of structure functions, there is a systematic error in this approach if both the underlying dynamics and the distribution of separation vectors are anisotropic. A straightforward angle-weighted approach is proposed, which resolves this systematic error. We appeal to readers that this approach can be applied to any scalar-based quantities, including third-order structure functions and so on, and should be relevant in more general applications even if one is not focused on the Helmholtz decomposition.

The paper flows as follows. In section 2, we state the basic definitions of second-order structure functions, and expand them in terms of azimuthal Fourier coefficients. The azimuthal Fourier transform converts 2D functions into isotropic and anisotropic modes, and we will analyze the modes systematically in later chapters. In section 3, we explain the potential systematic error from the traditional structure function

estimation approach that applies unweighted ensemble averages, and propose a straightforward angle-weighted approach to suppress it. Section 3 is self-containing and can be read alone if one is not primarily concerned with Helmholtz decompositions. In section 4, we derive the anisotropic Helmholtz decomposition formulae that in principle can diagnose any anisotropic modes of rotational or divergent structure functions. Notably, compared to the isotropic Helmholtz decomposition, this method does not require any additional observed fields. The form of anisotropy allowed in the derivation is quite general: the only constraint is that the cross covariance between ψ and ϕ needs to be either zero or at most isotropic. No more assumption is made other than stationarity and homogeneity. We then test and verify both the angle-weighted approach and the Helmholtz decomposition formulae on synthetic data in section 5, which shows excellent agreements with theoretical expectations. In section 6, we apply the new algorithms onto data from a recent surface drifter observational project that took place in the Gulf of Mexico. Some discussions and summary are offered in section 7.

2. Second-order structure functions

For each drifter pair the separation vector $\mathbf{r} = \Delta x \mathbf{e}_x + \Delta y \mathbf{e}_y$ connects the locations of the two drifters in a local tangent plane. We follow the usual convention that \mathbf{e}_x and \mathbf{e}_y point toward zonal and meridional directions, respectively. The velocity difference $\Delta \mathbf{u}$ between two drifters is decomposed into two components: Δu_L , the “longitudinal” component pointing along \mathbf{r} , and Δu_T , the “transversal” component pointing along $\mathbf{e}_z \times \mathbf{r}$ where \mathbf{e}_z is the vertical unit vector. The longitudinal and transversal second-order structure functions are then defined as

$$D_{LL}(\mathbf{r}) = \overline{\Delta u_L^2}, \quad D_{TT}(\mathbf{r}) = \overline{\Delta u_T^2}, \quad (2)$$

where $\overline{(\cdot)}$ denotes a suitable ensemble average. The assumptions of homogeneity and stationarity imply that these averages depend only on the separation vector \mathbf{r} . We also need the “cross” structure function

$$D_{LT}(\mathbf{r}) = \overline{\Delta u_L \Delta u_T}, \quad (3)$$

which will turn out to be crucial for our method. The velocity difference $\Delta \mathbf{u}$ can also be decomposed into $\Delta \mathbf{u}_R$, the velocity difference due to rotational motion induced by the streamfunction ψ in (1), and $\Delta \mathbf{u}_D$, the velocity difference induced by the potential function ϕ in (1):

$$\Delta \mathbf{u} = \Delta \mathbf{u}_R + \Delta \mathbf{u}_D. \quad (4)$$

The rotational and divergent structure functions, denoted as D_{RR} and D_{DD} , are

$$D_{RR}(\mathbf{r}) = \overline{\Delta u_R^2}, \quad D_{DD}(\mathbf{r}) = \overline{\Delta u_D^2}, \quad (5)$$

where $\Delta u_R = |\Delta \mathbf{u}_R|$ and $\Delta u_D = |\Delta \mathbf{u}_D|$. Under isotropy, it has been pointed out that the sum of D_{LL} and D_{TT} can be unambiguously expressed as a sum of D_{RR} and D_{DD} (Lindborg 2015):

$$D_{LL}(\mathbf{r}) + D_{TT}(\mathbf{r}) = D_{RR}(\mathbf{r}) + D_{DD}(\mathbf{r}). \quad (6)$$

We will later find out that the above still holds under anisotropic statistics. The principal goal is to diagnose the rotational and divergent structure functions $D_{RR}(\mathbf{r})$ and $D_{DD}(\mathbf{r})$ from observations of $\Delta u_L(\mathbf{r})$ and $\Delta u_T(\mathbf{r})$ without assuming isotropic statistics.

In subsequent analysis, we refer to second-order structure functions as “structure functions” for convenience. The only time higher-order structure functions are mentioned are in section 3, and we will be explicit about the order there. We will also work primarily in polar coordinates, referring to the polar angle α of the separation vector \mathbf{r} as the “separation angle,” and the magnitude of \mathbf{r} , denoted as r , as “separation distance.” The (second-order) structure functions considered in this work are *even* in \mathbf{r} , which means they have the same values at α and $\alpha + \pi$. So in the evaluation of structure functions from observations we can enforce $\Delta y \geq 0$ or $\alpha \in [0, \pi)$ without loss of generality.

We will systematically analyze 2D anisotropic functions through the lens of azimuthal Fourier series. Any smooth real function $f(r, \alpha)$ can be expanded into the azimuthal Fourier series

$$f(r, \alpha) = \sum_{n=0,1,2,\dots}^{\infty} f^{cn}(r) \cos(n\alpha) + f^{sn}(r) \sin(n\alpha), \quad (7)$$

where in (7), n are nonnegative integers and the azimuthal Fourier coefficients are

$$f^{c0} = \frac{1}{2\pi} \int_{-\pi}^{\pi} f(r, \alpha) d\alpha, \quad (8)$$

$$f^{cn} = \frac{1}{\pi} \int_{-\pi}^{\pi} f(r, \alpha) \cos(n\alpha) d\alpha, \quad n \neq 0, \quad (9)$$

$$f^{sn} = \frac{1}{\pi} \int_{-\pi}^{\pi} f(r, \alpha) \sin(n\alpha) d\alpha, \quad n \neq 0. \quad (10)$$

We also define the absolute value function when $n \neq 0$, which will be convenient when we compare modal amplitudes in figures.

$$f^{an}(r) \equiv \sqrt{f^{cn}(r)^2 + f^{sn}(r)^2}, \quad n \neq 0. \quad (11)$$

The (second-order) structure functions and covariance functions are all even by definition, so all odd-order modes are zero. Hence, we will only discuss the modes where n are even. If we assume a 2D function is isotropic, we are in fact truncating the expansion to the mode at $n = 0$. Conversely, as we allow for anisotropy in the statistics, we include higher modes at $n \geq 2$ in the azimuthal Fourier expansions of $D_{LL}(r, \alpha)$ and so on. Most derivations to appear in section 4 will be based on the azimuthal Fourier expansions, analyzing structure functions at each mode separately.

3. Angle-weighted structure function estimation

Anisotropic velocity statistics introduce a sampling issue that affects the estimation of all structure function modes,

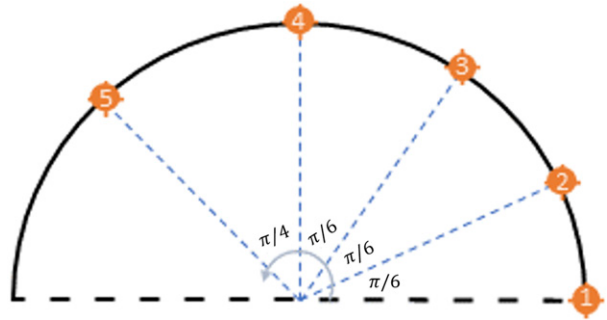


FIG. 1. Locations of the five drifter pairs distributed anisotropically at the same separation distance in the thought experiment. The underlying structure function (not plotted) is prescribed by (12), which is also anisotropic.

including the isotropic mode ($n = 0$). For example, consider estimating $D_{LL}^{c0}(r)$ at $r = r_i$ from a dataset. If the underlying $D_{LL}(r, \alpha)$ is *indeed* isotropic, then there would be no need to incorporate the *angle* distribution of separation vectors, and to estimate $D_{LL}^{c0}(r_i)$, one only needs to calculate a sample average of Δu_L^2 over all the drifter pairs whose separation *distances* fall into the distance bin around r_i . We call this the “unweighted approach.” To our knowledge, this is highly likely the popular practice so far, as we have never seen discussions on the angle distribution in previous literature when estimations of structure functions are introduced (e.g., Bennett et al. 2006; LaCasce 2016; Pearson et al. 2019). This approach is convenient and consistent with isotropy, but as we will see in the following thought experiment, if the underlying $D_{LL}(r, \alpha)$ is actually anisotropic, the unweighted approach based on isotropy introduces a systematic error.

Suppose the true $D_{LL}(r, \alpha)$ at $r = r_i$ is

$$D_{LL}(r_i, \alpha) = \sin(2\alpha) + 1 \quad (12)$$

and that there are 5 drifter pairs whose separation distances fall into the distance bin centered at $r = r_i$. We also assume a simple anisotropic arrangement of the separation vectors, as sketched in Fig. 1. The “true answer” for D_{LL}^{c0} is

$$D_{LL}^{c0}(r_i) = \frac{1}{\pi} \int_0^{\pi} [\sin(2\alpha) + 1] d\alpha = 1. \quad (13)$$

But in the unweighted approach D_{LL}^{c0} would be estimated simply as an average over the five observations:

$$\frac{1}{5} \left[0 + \sin\left(\frac{2\pi}{6}\right) + \sin\left(\frac{2\pi}{3}\right) + \sin\left(\frac{2\pi}{2}\right) + \sin\left(\frac{6\pi}{4}\right) \right] + 1 = 1.15,$$

which is significantly different from (13). What has gone wrong here is that the integral was biased toward angle regions where there were more observations.

This biasing error can be removed if we use a suitable *angle weighting* to counterbalance the empirical angle distribution. In the approach we are proposing here, we treat the evaluation of (13) as a numerical integration over a nonuniform grid.

In this example, the difference in the separation angles between the drifter pair at $\alpha = 0$ and the drifter pair at $\alpha = \pi/6$ is

$$\frac{1}{2\pi} \left\{ \left[\sin(0) + \sin\left(\frac{2\pi}{6}\right) \right] \times \frac{\pi}{6} + \left[\sin\left(\frac{2\pi}{6}\right) + \sin\left(\frac{2\pi}{3}\right) \right] \times \frac{\pi}{6} + \left[\sin\left(\frac{2\pi}{3}\right) + \sin\left(\frac{2\pi}{2}\right) \right] \times \frac{\pi}{6} + \left[\sin\left(\frac{2\pi}{2}\right) + \sin\left(\frac{2 \times 3\pi}{4}\right) \right] \times \frac{\pi}{4} + \left[\sin\left(\frac{2 \times 3\pi}{4}\right) + \sin(0) \right] \times \frac{\pi}{4} + 1 \right\} = 1.04, \quad (14)$$

so this approach yields the much better estimate 1.04 for (13). Higher modes such as

$$D_{LL}^{(n)}(r) = \frac{1}{2\pi} \int_0^\pi D_{LL}(r, \alpha) \cos n\alpha \, d\alpha, \quad (15)$$

can be estimated in the same fashion. For $n \gg 1$, noise in the observed $D_{LL}(r, \alpha)$ may be amplified by the highly oscillatory $\cos(n\alpha)$ in the evaluation of (15). In the applications to realistic data, we will only estimate the modes at $n = 0, 2$ and $n = 4$. Finally, in real data, occasionally, several drifter pairs in the ensemble may share a same, or almost identical separation vector. In that case, we chose to average observations from these drifter pairs, and treat the averaged value as a single point in the (r, α) space. Overall, this approach is elementary yet effective in our applications. We do not argue it is optimal, and an alternative approach is described in [appendix B](#).

The angle-weighted approach can be applied to the evaluations of any other scalar-based quantities. For example, to evaluate the zeroth mode of third-order structure functions, the only significant inconsistency with the thought experiment above is the oddness of third-order structure functions, which can be incorporated by making up an odd function to replace (13).

Last but not least, in the thought experiment, the weighted and unweighted approaches would give the *same* estimation for $D_{LL}^{(0)}(r)$ and so on if we modify our premises by making either the underlying $D_{LL}(r, \alpha)$, or the distribution of separation vectors to be instead isotropic. Here, by isotropic distribution, we mean that the five separation angles are equally

$\pi/6$, and so on. We use these empirical $\Delta\alpha$ values and apply a simple trapezoidal rule to (13):

spaced by $\pi/5$, so that the equally spaced angles span the whole angle range $[0, \pi)$. This leads to a practical rule: the angle weighting only makes a difference in the outcome when *both* the underlying 2D structure functions *and* the distribution of separation vectors are anisotropic.

4. Anisotropic Helmholtz decomposition

The angle-weighted approach described in the previous section allows us to estimate the velocity structure functions $D_{LL}(r, \alpha)$, $D_{TT}(r, \alpha)$, and $D_{LT}(r, \alpha)$ at any mode. In this section, we derive a set of formulae that relate the modes of the rotational and divergent structure functions to them, which is the key ingredient for a Helmholtz decomposition algorithm of sparse 2D observational data.

a. Helmholtz decomposition results

The BCF14 Helmholtz decomposition method for isotropic spectra can be adapted to isotropic structure functions ([Lindborg 2015](#)), yielding

$$D_{RR}(r) = D_{TT}(r) + \int_0^r [-D_{LL}(\tau) + D_{TT}(\tau)] \frac{d\tau}{\tau},$$

$$D_{DD}(r) = D_{LL}(r) - \int_0^r [-D_{LL}(\tau) + D_{TT}(\tau)] \frac{d\tau}{\tau}. \quad (16)$$

In this paper we show that for anisotropic flows this can be generalized to

$$D_{RR}(r, \alpha) = D_{TT}(r, \alpha) + \int_0^r \left[-D_{LL}(\tau, \alpha) + D_{TT}(\tau, \alpha) - \frac{\partial D_{LT}(\tau, \alpha)}{\partial \alpha} \right] \frac{d\tau}{\tau},$$

$$D_{DD}(r, \alpha) = D_{LL}(r, \alpha) - \int_0^r \left[-D_{LL}(\tau, \alpha) + D_{TT}(\tau, \alpha) - \frac{\partial D_{LT}(\tau, \alpha)}{\partial \alpha} \right] \frac{d\tau}{\tau}. \quad (17)$$

These formulas are exact under stationarity and homogeneity, provided that ψ and ϕ are either uncorrelated or correlated only via an isotropic function. In case ψ and ϕ are correlated via an anisotropic function, the formulas at the isotropic mode $n = 0$ are still valid. The azimuthal average of (17) brings back (16), which shows that (16) can be viewed as an equation for the $n = 0$ mode. The implied azimuthal average brings in the angle-weighting issue discussed in [section 3](#).

We have not been able to derive (17) in a straightforward fashion, instead its Fourier mode form was guessed and then verified using Wolfram Mathematica. The corresponding

codes are located in the online supplemental material. To do this we first express the structure functions in terms of the velocity covariances and then use the covariances of the streamfunction ψ and velocity potential ϕ to find the divergent and rotational components, respectively. This is sketched now.

b. Expressions for velocity structure functions

By definition (see [section 2](#)) we have

$$\Delta u_L = \Delta u \cos(\alpha) + \Delta v \sin(\alpha), \quad (18)$$

$$\Delta u_T = -\Delta u \sin(\alpha) + \Delta v \cos(\alpha), \tag{19}$$

where (u, v) are zonal and meridional velocities. For the velocity structure functions this yields

$$D_{LL} = \overline{\Delta u^2} \cos^2(\alpha) + \overline{\Delta v^2} \sin^2(\alpha) + \overline{\Delta u \Delta v} \sin(2\alpha), \tag{20}$$

for example. We can then use the standard relations

$$\begin{aligned} \overline{\Delta u \Delta v}(\mathbf{r}) &= 2\overline{uv} - C_{uv}(\mathbf{r}) - C_{uv}(-\mathbf{r}), \\ \overline{\Delta u^2}(\mathbf{r}) &= 2[\overline{u^2} - C_u(\mathbf{r})], \\ \overline{\Delta v^2}(\mathbf{r}) &= 2[\overline{v^2} - C_v(\mathbf{r})], \end{aligned} \tag{21}$$

to bring in C_u, C_v , the covariance functions of u and v respectively, and also the cross covariance $C_{uv}(\mathbf{r})$. As a reminder, the covariance and cross-covariance functions are defined as

$$C_u(\mathbf{r}) = \overline{u(\mathbf{r}_0)u(\mathbf{r}_0 + \mathbf{r})}, \quad C_{uv}(\mathbf{r}) = \overline{u(\mathbf{r}_0)v(\mathbf{r}_0 + \mathbf{r})}, \tag{22}$$

where we have assumed zero-mean fields, and as a consequence of homogeneity, the location variable \mathbf{r}_0 that denotes the initial point vanishes after ensemble averaging. $C_u(\mathbf{r})$ or $C_v(\mathbf{r})$ are always even, but $C_{uv}(\mathbf{r})$ need not be. Henceforth we use the letter C to denote covariance or cross-covariance functions, depending on whether it is adorned by one or two subscripts. With manipulations similar to [appendix A](#) in [BKT17](#), we can further relate the above to the covariance and cross-covariance functions of ψ and ϕ :

$$C_u = -\frac{\partial^2 C_\phi}{\partial x^2} - \frac{\partial^2 C_\psi}{\partial y^2} + \frac{\partial^2 C_{\psi\phi}}{\partial x \partial y} + \frac{\partial^2 C_{\phi\psi}}{\partial x \partial y}, \tag{23}$$

$$C_v = -\frac{\partial^2 C_\phi}{\partial y^2} - \frac{\partial^2 C_\psi}{\partial x^2} - \frac{\partial^2 C_{\psi\phi}}{\partial x \partial y} - \frac{\partial^2 C_{\phi\psi}}{\partial x \partial y}, \tag{24}$$

$$C_{uv} = -\frac{\partial^2 C_\phi}{\partial x \partial y} + \frac{\partial^2 C_\psi}{\partial x \partial y} + \frac{\partial^2 C_{\psi\phi}}{\partial y^2} - \frac{\partial^2 C_{\phi\psi}}{\partial x^2}, \tag{25}$$

where we used $\mathbf{r} = (x, y)$ for simplicity here. Now, in our theory we allow for arbitrary $C_\phi(\mathbf{r})$ and $C_\psi(\mathbf{r})$, but restrict $C_{\psi\phi}(\mathbf{r})$ to be isotropic (or zero), i.e., it can only be a function of the separation distance $r = |\mathbf{r}|$. Relaxations of this extra assumption will be discussed in [section 4e](#), but for now we stick to this assumption for simplicity. Hence $C_{\psi\phi}(\mathbf{r}) = C_{\phi\psi}(\mathbf{r})$ and [\(23\)–\(25\)](#) can be shortened. The velocity correlation C_{uv} is even too, which simplifies [\(21\)](#) to

$$\overline{\Delta u \Delta v} = 2(\overline{uv} - C_{uv}). \tag{26}$$

Combining these equations, and with help from Wolfram Mathematica, we can finally express D_{LL}, D_{TT} , and D_{LT} in terms of $C_\phi(\mathbf{r}), C_\psi(\mathbf{r})$ and $C_{\psi\phi}(\mathbf{r}) = C_{\phi\psi}^0(r)$. For the Fourier modes this yields

$$D_{LL}^0 = \overline{u^2} + \overline{v^2} + 2(C_\phi^0)'' + \frac{2(C_\psi^0)'}{r}, \tag{27}$$

$$D_{LL}^n = \mathbf{1}_{n=2}(\overline{u^2} - \overline{v^2}) + 2(C_\phi^{cn})'' - \frac{2n^2 C_\psi^{cn}}{r^2} + \frac{2(C_\psi^{cn})'}{r}, \quad n \geq 2; \tag{28}$$

$$D_{LL}^{sn} = \mathbf{1}_{n=2}(2\overline{uv}) + 2(C_\phi^{sn})'' - \frac{2n^2 C_\psi^{sn}}{r^2} + \frac{2(C_\psi^{sn})'}{r}, \quad n \geq 2; \tag{29}$$

$$D_{TT}^{c0} = \overline{u^2} + \overline{v^2} + \frac{2(C_\phi^{c0})'}{r} + 2(C_\psi^{c0})''; \tag{30}$$

$$D_{TT}^{cn} = \mathbf{1}_{n=2}(-\overline{u^2} + \overline{v^2}) + \frac{2(C_\phi^{cn})'}{r} - \frac{2n^2 C_\psi^{cn}}{r^2} + 2(C_\psi^{cn})'', \quad n \geq 2; \tag{31}$$

$$D_{TT}^{sn} = \mathbf{1}_{n=2}(-2\overline{uv}) + \frac{2(C_\phi^{sn})'}{r} - \frac{2n^2 C_\psi^{sn}}{r^2} + 2(C_\psi^{sn})'', \quad n \geq 2; \tag{32}$$

$$D_{LT}^{c0} = -\frac{2(C_{\psi\phi}^{c0})'}{r} + 2(C_{\psi\phi}^{c0})''; \tag{33}$$

$$\begin{aligned} D_{LT}^{cn} &= \mathbf{1}_{n=2}(2\overline{uv}) + \frac{2n(C_\phi^{cn})'}{r} - \frac{2n C_\psi^{cn}}{r^2} \\ &\quad + \frac{2n C_{\psi\phi}^{cn}}{r^2} - \frac{2n(C_{\psi\phi}^{cn})'}{r}, \quad n \geq 2; \end{aligned} \tag{34}$$

$$\begin{aligned} D_{LT}^{sn} &= \mathbf{1}_{n=2}(-\overline{u^2} + \overline{v^2}) - \frac{2n(C_\phi^{sn})'}{r} + \frac{2n C_\psi^{sn}}{r^2} \\ &\quad - \frac{2n C_{\psi\phi}^{sn}}{r^2} + \frac{2n(C_{\psi\phi}^{sn})'}{r}, \quad n \geq 2. \end{aligned} \tag{35}$$

Here primes denote differentiation with respect to r and $\mathbf{1}_{n=2} = 1$ if $n = 2$ and zero otherwise; note that there are terms peculiar to the $n = 2$ mode. If all covariance terms diminish at a decorrelation scale, which presumably should be the limit $r \rightarrow \infty$, we can extract the decorrelation limits

$$\lim_{r \rightarrow \infty} D_{LL}^{c0} = \lim_{r \rightarrow \infty} D_{TT}^{c0} = \overline{u^2} + \overline{v^2}, \quad \lim_{r \rightarrow \infty} D_{LT}^{c0} = 0, \tag{36}$$

$$\begin{aligned} \lim_{r \rightarrow \infty} D_{LL}^{sn} &= \lim_{r \rightarrow \infty} D_{TT}^{sn} = \lim_{r \rightarrow \infty} D_{LT}^{sn} \\ &= \mathbf{1}_{n=2} \sqrt{(\overline{u^2} - \overline{v^2})^2 + (2\overline{uv})^2}. \end{aligned} \tag{37}$$

We will check if such limiting behaviors are indeed satisfied in synthetic and observational data. We also note here that $D_{LL}(r, \alpha) = D_{TT}(r, \alpha)$ at decorrelation scale, which is a generalization of a similar result in the isotropic case ([Lindborg 2015](#)).

c. Nonzero $C_{\psi\phi}(r)$ and ‘‘spirality’’ of the flow

It follows from [\(33\)–\(35\)](#) that $D_{LT}(\mathbf{r}) = 0$ if the correlation functions of ψ and ϕ are isotropic and their cross correlation is zero, which is likely the reason why D_{LT} was usually ignored in previous work. On the other hand, [\(33\)](#) shows that in general $D_{LT}^{c0}(r) \neq 0$ even if ψ and ϕ are correlated only by an isotropic term, which is the case that we allow for in the present theory. An intriguing situation arises if *all* correlation functions are isotropic yet $D_{LT}^{c0} \neq 0$ because $C_{\psi\phi}^{c0} \neq 0$. This implies that there is an isotropic handedness involved in the statistical description of the flow, i.e., the flow statistics can distinguish between a clockwise and a counterclockwise rotation of the velocity along the separation vector \mathbf{r} .

This makes sense physically, given that the Coriolis force provides precisely this handedness, but it is puzzling at first sight from a mathematical point of view: if all correlation functions are isotropic, how can the preference to turn clockwise, say, be

encoded in the statistics? The answer to that comes from the observation that ψ and ϕ behave differently under a reflection of the flow across a line such as the y axis: in this case ϕ remains the same but ψ changes sign. In physical terms, ϕ behaves like a scalar but ψ like a pseudoscalar, a consequence of the obvious handedness involved in the definition of ψ . Hence a nonzero correlation between ϕ and ψ implies a lack of reflection symmetry of the flow statistics, leading to $D_{LT}^{c0}(r) \neq 0$.

Notably, one can check with similar steps as before that the cross covariance between vertical vorticity ζ and horizontal divergence χ is directly related to that between ψ and ϕ via $C_{\zeta\chi} = \nabla_h^4 C_{\psi\phi}$, where ∇_h^2 is the horizontal Laplacian operator. Hence if $C_{\psi\phi}$ behaves in a way that makes $C_{\zeta\chi}$ positive, then cyclonic vorticity is correlated with flow divergence and vice versa. The resultant flow pattern will exhibit a distinct ‘‘spirality,’’ with outward or inward spirals preferentially associated with cyclones or anticyclones, respectively [W. Young 2020, personal communication; see also Zhurbas et al. (2019) for recent observations of tracer spirals]. Such spirality obviously implies a lack of reflectional symmetry of the flow statistics.

d. Anisotropic Helmholtz decomposition

A crucial observation from (27)–(32) is that any mode of the sum ($D_{LL} + D_{TT}$) is a linear combination of terms related only to C_ϕ and C_ψ , and the cross terms $C_{\psi\phi}$ or $C_{\phi\psi}$ play no role. This means that D_{RR} or D_{DD} , whose definitions are essentially ‘‘velocity structure functions due to rotational or divergent motions,’’ can unambiguously be told apart in their contribution to ($D_{LL} + D_{TT}$) if we have full knowledge of ψ and ϕ : we can simply evaluate them by retaining the terms induced by ψ or ϕ , respectively. Formally,

$$D_{RR} = D_{LL} + D_{TT} \quad \text{with } \phi \text{ taken as 0,} \quad (38)$$

and

$$D_{DD} = D_{LL} + D_{TT} \quad \text{with } \psi \text{ taken as 0.} \quad (39)$$

To illustrate how to use (38) and (39), at $n = 0$, we have by summing up (27) and (30) and taking $\phi = 0$

$$D_{RR}^{c0} = A + \frac{2(C_\psi^{c0})'}{r} + 2(C_\psi^{c0})'', \quad (40)$$

where the constant A is determined from the zero boundary condition of structure functions at $r = 0$. The other modes of D_{RR} and D_{DD} can be similarly evaluated. Resubstituting from (27)–(35) as needed we can then verify the following integral relationships

$$\begin{aligned} D_{RR}^n(r) &= D_{TT}^n(r) + \int_0^r \left[\frac{-D_{LL}^n(\tau) + D_{TT}^n(\tau)}{\tau} - n \frac{D_{LT}^n(\tau)}{\tau} \right] d\tau, \\ D_{RR}^m(r) &= D_{TT}^m(r) + \int_0^r \left[\frac{-D_{LL}^m(\tau) + D_{TT}^m(\tau)}{\tau} + n \frac{D_{LT}^m(\tau)}{\tau} \right] d\tau, \\ D_{DD}^n(r) &= D_{LL}^n(r) - \int_0^r \left[\frac{-D_{LL}^n(\tau) + D_{TT}^n(\tau)}{\tau} - n \frac{D_{LT}^n(\tau)}{\tau} \right] d\tau, \\ D_{DD}^m(r) &= D_{LL}^m(r) - \int_0^r \left[\frac{-D_{LL}^m(\tau) + D_{TT}^m(\tau)}{\tau} + n \frac{D_{LT}^m(\tau)}{\tau} \right] d\tau. \end{aligned} \quad (41)$$

These were the equations found first by guesswork and then verified in Wolfram Mathematica. The guess was inspired by $D_{LT} \neq 0$ for $n > 0$ under anisotropy, and was stumbled upon by listing and observing all the separate modes that are shown in section 4b. Summing the Fourier series then yields the compact relations in (17).

The terms on the RHS in formulae (41) can be estimated from data by the angle-weighted approach described in section 3, which works for sparse 2D observations, as long as the mode number n is not too high to exaggerate observational noises. In practice, we will stop at $n = 4$.

At the mode $n = 0$, the Helmholtz decomposition formulae (41) are identical to the Helmholtz decomposition formulae under assumption of isotropy (16). We stress, however, that although the Helmholtz decomposition formulae are the same at the zeroth modes, the angle-weighted approach to estimate the input functions $D_{LL}^{c0}(r)$, $D_{TT}^{c0}(r)$, and $D_{LT}^{c0}(r)$ described in section 3 could still render different outcomes.

e. Consequences of anisotropic $C_{\psi\phi}$

Even though the relations (27)–(32) were derived under the assumption that $C_{\psi\phi}$ is isotropic, we found with similar steps that even if $C_{\psi\phi}(r, \alpha)$ contains anisotropic modes, the sum ($D_{LL} + D_{TT}$) is still always a linear combination of terms related to C_ϕ and C_ψ , which means (6), (38) and (39) are valid and a Helmholtz decomposition should still be a well-defined problem in the sense that it can always be achieved if full knowledge of C_ψ and C_ϕ is available. The remaining question is then how to achieve the Helmholtz decomposition if the only inputs available are modes of velocity structure functions.

Apparently, the assumption that $C_{\psi\phi}$ is isotropic can easily be relaxed to allow for *odd* Fourier modes in $C_{\psi\phi}$. With similar steps as above we find that the expressions for the velocity structure function modes from (27) to (35) turn out exactly the same, and hence (41) hold as is. We are not aware of any particularly useful implications of this result yet, and hence we stick to the stricter assumption of isotropy for simplicity.

The troubling case is when $C_{\psi\phi}$ contains *even and nonzero* Fourier modes (i.e., $n = 2, 4, 6, \dots$). In this case, (27)–(35) turn out different at $n \geq 2$ in a way that makes the formulas (41) invalid at $n \geq 2$. However, at $n = 2$, we find that the modes D_{LL}^{c0} , D_{TT}^{c0} and D_{LT}^{c0} happen to stay unchanged: all the modes at $n > 0$ in $C_{\psi\phi}$ do not leave fingerprints on D_{LL}^{c0} , D_{TT}^{c0} and D_{LT}^{c0} . Hence, the Helmholtz decomposition formulas (41) at $n = 0$ holds even in this troubling case. We attach the relevant derivations, which follow similar steps as in sections 4b and 4d, in the illustrated code provided in the supplemental material.

This may indeed be a useful result: the current Helmholtz decomposition formulas (41) are always valid at the mode $n = 0$ no matter what form $C_{\psi\phi}$ takes. This means that in a dataset, if anisotropic modes are diagnosed to be magnitudes weaker than the isotropic modes, then the Helmholtz decomposition, then dominated by the isotropic modes, would be valid even if $C_{\psi\phi}$ violates our assumption. In the Lagrangian Submesoscale Experiment (LASER) data application, we have not found a good chance to apply this result as anisotropic modes rarely turn out to be more than 10 times smaller than the isotropic modes, but it is still potentially useful in other datasets.

We also note that the isotropy of $C_{\psi\phi}$ is already a weaker assumption than the uncorrelatedness between ψ and ϕ [i.e., $C_{\psi\phi}(\mathbf{r}) = 0$], which has been made in some preceding works (BCF14; Calies et al. 2014). As derived in BCF14, the uncorrelated case is at least consistent with a classic idealized scenario: a superposition of purely geostrophic flow and linear inertia–gravity waves. To make the theory more applicable it would be desirable to incorporate general forms of $C_{\psi\phi}$. This is left as future work.

5. Synthetic examples

We have developed a code for (17) and (41) that includes suitable angle weighting and here we test it on two synthetic examples. For these examples the “true answers” for D_{RR} and D_{DD} should be known. We achieve this by setting up the underlying 2D power and cross spectrum of ψ and ϕ which are easily related to both the velocity fields and D_{RR} and D_{DD} . These true answers for D_{RR} and D_{DD} are to be reconstructed from velocity “observations” on synthetic drifters.

The 2D power spectrum of $\psi(x, y)$, denoted as $S_\psi(k, l)$, is the 2D Fourier transform of the covariance function $C_\psi(x, y)$, and the 2D cross spectrum of $\psi(x, y)$ and $\phi(x, y)$, denoted as $S_{\psi\phi}(k, l)$, is the 2D Fourier transform of the cross covariance $C_{\psi\phi}(x, y)$. The power spectra and cross spectra are also known to be related to the Fourier modes of individual fields via (Yaglom 2004)

$$S_\psi(k, l) = \frac{|\hat{\psi}(k, l)|^2}{L^2}, \quad S_{\psi\phi}(k, l) = \frac{\hat{\psi}^*(k, l)\hat{\phi}(k, l)}{L^2}, \quad (42)$$

where $\hat{\psi}(k, l)$ and $\hat{\phi}(k, l)$ denote the 2D Fourier coefficients of $\psi(x, y)$ and $\phi(x, y)$, and L is the domain length in real space (x, y) , fixed here at $L = 250$ km.

Both examples feature the band-limited spectra

$$S_\psi(k, l) = C_S(p k^2 + l^2)^{-3/2} K^{-2}, \quad S_\phi(k, l) = C_H K^{-5}, \quad (43)$$

$$S_{\psi\phi} = C_P K^{-5}, \quad K = \sqrt{k^2 + l^2}. \quad (44)$$

Outside the wavenumber interval $2\pi/(100 \text{ km}) < K < 2\pi/(1 \text{ km})$ the spectra are zero. The corresponding one-dimensional kinetic energy spectra along k due to ψ or ϕ are both proportional to power decay laws k^{-2} within the interval.

a. Isotropic example with strong correlation

In the first example $p = 1$, rendering the input spectra isotropic. The constants C_S, C_H are fixed so that the root-mean-square velocities in the domain due to ψ or ϕ are 0.2 and 0.1 m s^{-1} , respectively. The constant C_P is set to be $0.9\sqrt{C_S C_H}$. Under this configuration, the Cauchy–Schwartz inequality condition

$$|S_{\psi\phi}(k, l)|^2 \leq S_\psi(k, l) S_\phi(k, l) \quad (45)$$

holds at all wavenumbers, making this a realizable spectrum. In this example the magnitudes of $S_{\psi\phi}(k, l)$, $S_\psi(k, l)$ and $S_\phi(k, l)$ are all comparable to each other: in 2-norm, $S_{\psi\phi}(k, l)$ is roughly twice as big as $S_\phi(k, l)$ and a half as big as $S_\psi(k, l)$. To construct

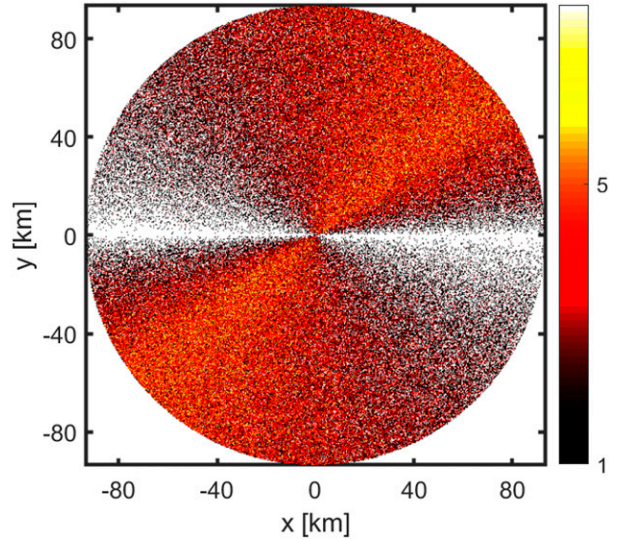


FIG. 2. Histogram of drifter positions (x, y) in synthetic examples (sections 5a and 5b). The polar angle of drifter locations follows a double-triangular distribution in the interval $[0, 2\pi]$, peaking at $\pi/5$ and $6\pi/5$. The square of the radial coordinate of drifter locations follows a uniform distribution in the interval $[0, (3L/8)^2]$. The histogram is plotted with 500×500 bins.

the true answers, we first directly calculate from these model spectra the corresponding 2D structure functions $D_{LL}(r, \alpha)$, $D_{TT}(r, \alpha)$, $D_{LT}(r, \alpha)$ from the general relations (21)–(25). Also similar to section 4d, the true answers of $D_{RR}(r, \alpha)$ and $D_{DD}(r, \alpha)$ are evaluated by summing up (23) and (24), and deleting all the terms involving $C_\phi(r, \alpha)$ and $C_\psi(r, \alpha)$, respectively. With the method described in appendix A, we evaluate the $n = 0$, $n = 2$, and $n = 4$ modes directly from these 2D structure functions.

We generate 1000 independent random snapshots of the velocity fields that are consistent with the assigned spectra S_ψ , S_ϕ , and $S_{\psi\phi}$, and for each of those snapshots we randomly generate 400 independent locations in the real domain, which we assign as drifter locations. The large sample number makes statistical noise almost invisible in figures. We purposefully ensure that the drifter locations are anisotropically distributed, by demanding that the polar angles of drifter locations concentrate around $\pi/5$ and $6\pi/5$, as sketched in the histogram Fig. 2. It is the separation vectors of these drifters, not the positions of each drifter themselves, that are directly required in calculations of structure function reconstructions. We present a histogram of the separation vectors $(\Delta x, \Delta y)$ with $\Delta y \geq 0$ from all the drifter pairs in Fig. 3. The distribution of separation vectors is anisotropic too under our configuration.

At separation distances larger than about 84 km, marked by the semicircle in figure Fig. 3, there are nearly no drifter pairs at a significantly wide gap in angles. To have a reasonable estimate of azimuthal Fourier modes, which are in essence angle integrations, the observations need to have a reasonable coverage over angles. Hence, we will only calculate the modes of structure functions with r up to $r = 84$ km in the angle-weighted approach described in section 3. In the traditional unweighted

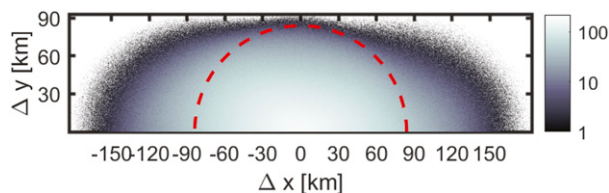


FIG. 3. Histogram of separation vectors $(\Delta x, \Delta y)$ in synthetic example (section 5a). The dashed half-circle marks the radius of 84 km, beyond which there are significant gaps in the distribution of separation angles. The histogram is plotted with 200×200 bins.

approach to estimate structure functions under isotropy, the angle distributions are not investigated, and these gaps in angles would likely not be detected or regarded as a concerning factor. Hence, when we conduct the reconstructions with the traditional unweighted approach, the modes of structure functions are calculated up to a higher r .

We compute the random velocity fields from samples of $\hat{\psi}(k, l)$ and $\hat{\phi}(k, l)$ that follow a multivariate Gaussian distribution consistent with (44). To ensure the correct cross correlation we follow a standard strategy (Rasmussen 2003): $[\hat{\psi}(k, l), \hat{\phi}(k, l)]$ are drawn as a complex bivariate sample that follows the two-variable Gaussian distribution with mean zero and covariance matrix

$$\Sigma = \begin{bmatrix} S_{\psi}(k, l) & S_{\psi\phi}(k, l) \\ S_{\phi\psi}(k, l) & S_{\phi}(k, l) \end{bmatrix}. \quad (46)$$

Numerically, we compute the Cholesky decomposition of Σ , which is bound to be symmetric and positive definite from (45), finding \mathbf{A} such that $\mathbf{A}\mathbf{A}^T = \Sigma$, and draw a random vector $\mathbf{z} = (z_1, z_2)^T$, where z_1 and z_2 are independent samples from standard normal distributions. The product $\mathbf{A}\mathbf{z}$ would then have the zero mean and the covariance matrix Σ as we desired. If either $S_{\psi}(k, l)$ or $S_{\phi}(k, l)$ is zero then so is $S_{\psi\phi}(k, l)$, meaning that $\hat{\psi}(k, l)$ and $\hat{\phi}(k, l)$ are uncorrelated at this wavenumber. We can then just sample $\hat{\psi}(k, l)$ and $\hat{\phi}(k, l)$ separately from $S_{\psi}(k, l)$ and $S_{\phi}(k, l)$, assuming single-variable zero-mean Gaussian distributions.

Afterward, we enforce the reality condition on $\hat{\psi}(k, l)$ and $\hat{\phi}(k, l)$ so that their inverse Fourier transforms are purely real and normalize the samples accordingly.

With $\hat{u}(k, l)$ and $\hat{v}(k, l)$ sampled, we can then numerically evaluate the velocities at each drifter location (x, y) by the inverse Fourier series:

$$u(x, y) = \frac{1}{L^2} \sum_{k,l} \hat{u}(k, l) e^{i(kx+ly)}. \quad (47)$$

In our application, we directly evaluate the sum (47) instead of applying a FFT algorithm, as the drifter locations presented in Fig. 2 do not fall on a regular grid. For our purpose this is not too costly, as we only evaluate $u(x, y)$ on 400 points in each snapshot.

The binning in r is set so that the number of drifter pairs in each bin is about the same. In the results presented in this section, we apply 256 bins in r , and each bin contains about 30 500 pairs of drifters. Varying the number of bins by a factor of 4 did not significantly change the outcomes. We then apply both the angle-weighted approach and the unweighted approach described in section 3 to evaluate different modes of $D_{LL}(r, \alpha)$, $D_{TT}(r, \alpha)$, and $D_{LT}(r, \alpha)$ and compare the outcomes.

We note that although the underlying true answers are all isotropic, we do not “tell” our algorithms that they are a priori, and all the inputs are the positions and velocity recordings of the synthetic drifters. At modes $n > 0$, all the structure functions considered should be zero, and we intend to test if the synthetic drifters can recover these zero values.

As shown in figure Fig. 4, the reconstructed velocity structure function are in agreement with the true answers at the $n = 0$, $n = 2$, and $n = 4$ modes. At $n = 2$ and $n = 4$ modes, the synthetic drifters recover the zero values. The decorrelation limits of the $n = 0$ modes, estimated via (36) and (37), also seem consistent with the behaviors of the true answers at larger r . In this example, there is a strong correlation between ψ and ϕ , which is the cause for nonzero values in $D_{LT}^{c0}(r)$ that are comparable in magnitude with $D_{LL}^{c0}(r)$ or $D_{TT}^{c0}(r)$. We will apply these reconstructed structure function modes to diagnose the corresponding modes of the

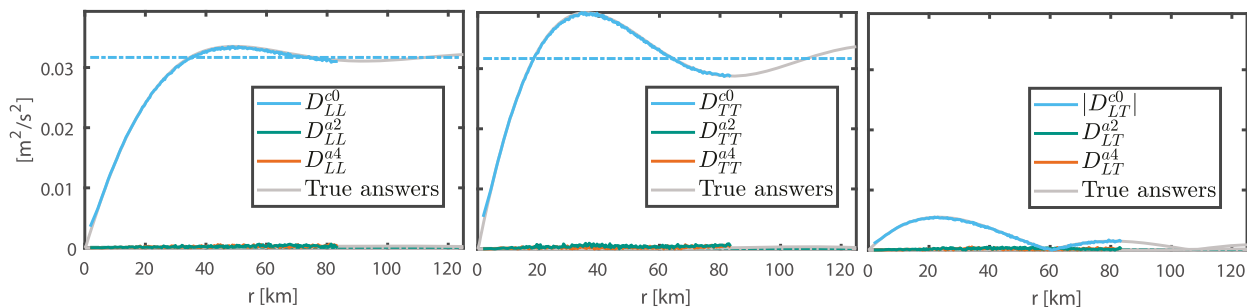


FIG. 4. The $n = 0$, $n = 2$, and $n = 4$ modes of (left) D_{LL} , (center) D_{TT} , and (right) D_{LT} in the first synthetic example where underlying structure functions are isotropic. Note that for anisotropic modes, the absolute value of the modes defined in (11) are presented. The grey lines mark the “true answers” for all the presented modes, which are evaluated directly from 2D structure functions corresponding to the underlying spectra, and colored lines mark the reconstructions from synthetic drifter observations under the angle-weighted approach. The dash-dot lines mark the decorrelation limits of different modes at $r \rightarrow \infty$ that is estimated from (36) and (37). Note that the plots in synthetic experiments do not use logarithmic scales, contrary to popular practice on observational data.

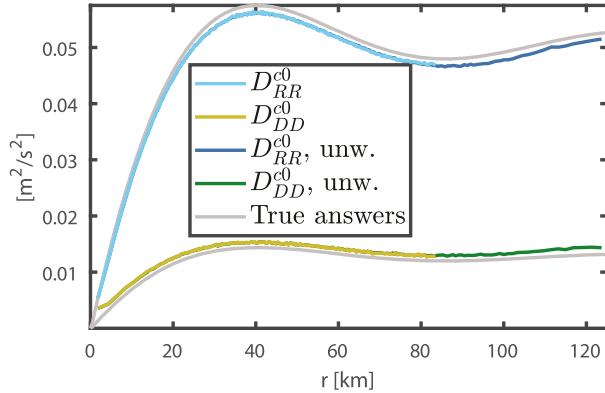


FIG. 5. Helmholtz decomposition of second-order structure functions at the $n = 0$ mode in the first synthetic example. The gray lines mark the “true answers” for all the presented modes, evaluated directly from 2D structure functions. Lines marked with text “unw.” in the legends represent modes reconstructed from synthetic drifters under the unweighted approach, and the rest of the lines are reconstructed under the angle-weighted approach. In this example the weighted and unweighted outcomes are identical at the overlapping distances.

rotational and divergent structure functions via the Helmholtz decomposition formulas (41).

As noted in section 3, the angle weighting would make a difference only when both the distribution of separation vectors and the underlying functions are anisotropic. In this synthetic example, the underlying structure functions are isotropic. Thus, the approaches with or without the angle weighting are both expected to correctly reconstruct the structure functions, even though the calculation processes are different.

In Fig. 5, we present the $n = 0$ modes of D_{RR} and D_{DD} . The presentations of the $n = 2$ or $n = 4$ modes for $D_{RR}(r, \alpha)$ and $D_{DD}(r, \alpha)$ are skipped here, as they all turn out close to zero. We find that the reconstructed structure functions using both the angle-weighted and the unweighted approach are in agreements with the true answer, which should be expected, as the error in the reconstructed velocity structure functions are shown small in Fig. 4. The small error at r around 40–80 km, which may be noticeable to a careful eye, are well bounded by 10%. It is caused by numerical integration of a noisy function,

and decreases when we change the bin sizes in r to be more optimal. In summary, from this example, we have demonstrated that the reconstruction of different modes of velocity structure functions as well as the rotational/divergent structure functions behave as we expected under isotropy in the presence of a strong cross spectrum $S_{\psi\phi}(k, l)$. As all the structure functions are isotropic here, at valid separation distances the angle weighting does not make any difference.

b. Anisotropic example

The main goal of this example is to test if our reconstruction algorithm works in the existence of strong anisotropy, and to demonstrate that angle weighting can be crucial in such scenarios. The general flow of this example is similar to the previous example, and the major change is in the constant p in (44): to introduce anisotropy, we pick p to be 5 in this example. The value 5 was chosen arbitrarily. In order for the inequality (45) to still hold, we also modify the constant C_p into $0.9\sqrt{5^{-3/2}}C_S C_H$. Under this configuration, the cross spectrum $S_{\psi\phi}(k, l)$ would turn out weaker compared to the previous example; in 2-norm, $S_{\psi\phi}(k, l)$ is roughly half as big as $S_\phi(k, l)$, and 15% as big as $S_\psi(k, l)$. The true answers and synthetic drifters are sampled in the same way as in the previous example.

We present the reconstructions of the $n = 0, n = 2$, and $n = 4$ modes of velocity structure functions in this example in Fig. 6. The reconstructions of all these modes from the angle-weighted approach appear successful. In Fig. 7, we present the modes of $D_{RR}(r, \alpha)$ and $D_{DD}(r, \alpha)$. The reconstructions obtained using the angle-weighted approach again agrees with the true answers, but the reconstructions obtained with the unweighted approach diverge significantly. At around $r = 100$ km, there is a crossover of $D_{RR}^{c0}(r)$ and $D_{DD}^{c0}(r)$ in the outcome of the unweighted approach, which could mislead one into believing a fundamentally different underlying dynamics from the true answers. This illustrates a main point of this example: the angle weighting could indeed be important when both the underlying structure functions and the distribution of separation vectors are anisotropic.

6. Application to LASER data

We now demonstrate the Helmholtz decomposition with angle weighting by applying it to a well-studied dataset.

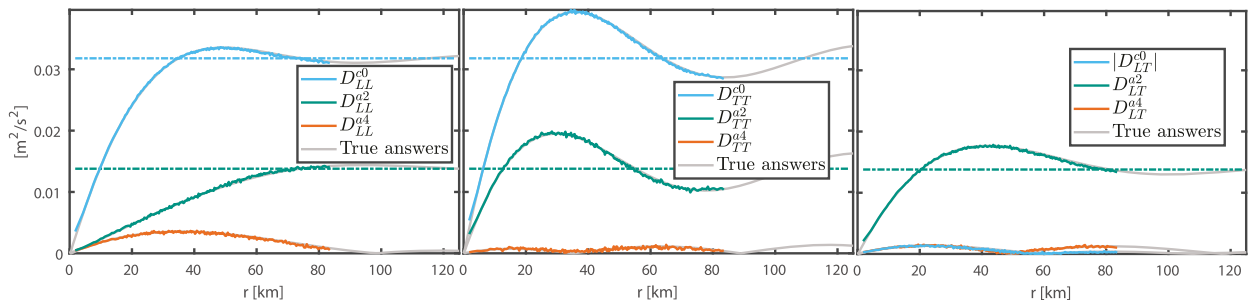


FIG. 6. As in Fig. 4, but for the second synthetic example instead.

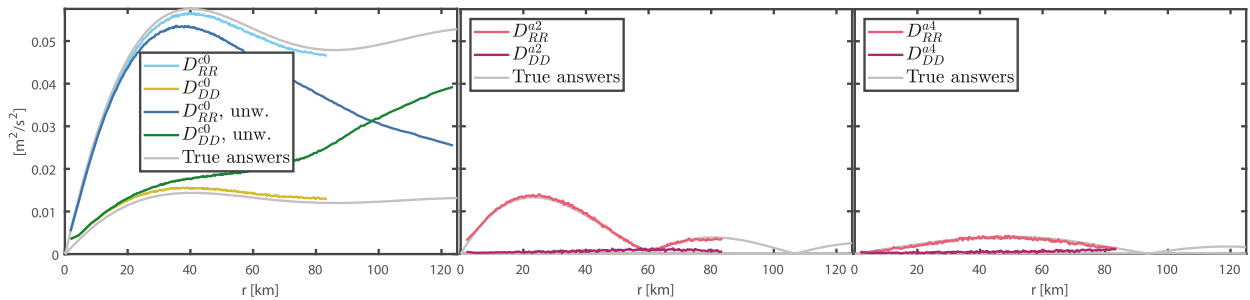


FIG. 7. Helmholtz decomposition of second-order structure functions at (left) $n = 0$, (center) $n = 2$, and (right) $n = 4$ modes in the second synthetic example. The line legends in the left panel are the same as in Fig. 5. In the center and right panels, the gray lines still mark the “true answers,” and the colored lines are reconstructed under the angle-weighted approach.

The primary aim is to show that the new method is easy to use and builds naturally on previous methods, rather than to find new physical effects in this particular dataset.

a. Data and methods

The LASER took place near the site of the *Deepwater Horizon* oil spill in the northern Gulf of Mexico. In this work we restrict the attention to the >1000 Consortium for Advanced Research on Transport of Hydrocarbon in the Environment (CARTHE)-type drifter units, which were drogued at 0.5 m and reported their positions through GPS tracking every 5 min for about 3 months, covering the period from 21 January through 30 April 2016. Among the released drifters, 840 were densely deployed around 28°–29°N and 87°–89°W, intended to monitor the structure of frontal lines, and the remaining drifters were deployed to provide a contextual map of the mesoscale flows during the operation (Novelli et al. 2017, 20–21). Among all the positions reported, 95% have an error of 10 m or less (Novelli et al. 2017, p.4).

We use the processed data product (D’Asaro et al. 2017), where the positions are low-pass filtered and interpolated to uniform 15 min intervals. The trajectories are separated at drogue loss, which are detected for deletion by transmission data and comparison of neighboring drifter velocities (Haza et al. 2018). In this work, we do not discard or attach weight on any specific deployments or snapshots for simplicity.

Shown in Fig. 8 is the histogram of the locations of drifters from all available observations. We will analyze in section 6b observations from all the areas covered in the dataset, and in section 6c four different spatial subregions marked in the right panel of Fig. 8.

Denoting the longitude and the latitude of two drifters in a drifter pair as (λ_1, θ_1) and (λ_2, θ_2) , the meridional separation Δy and the zonal separation Δx of the drifter pair are evaluated as

$$\Delta y = R(\theta_2 - \theta_1), \quad (48)$$

$$\Delta x = R(\lambda_2 - \lambda_1)[\cos(\theta_2) + \cos(\theta_1)]/2, \quad (49)$$

where R is the radius of Earth. We have tested that the results are insensitive to other reasonable choices such as

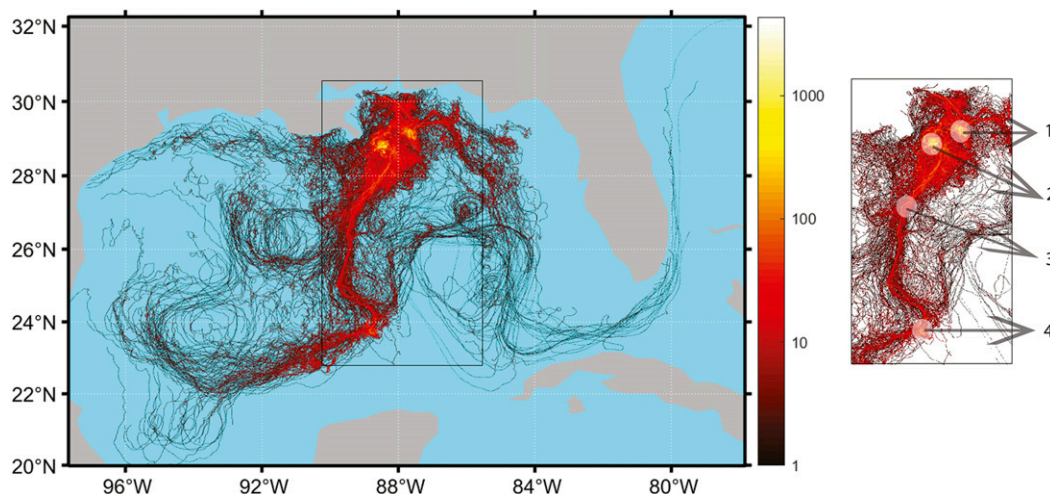


FIG. 8. (left) Histogram of drifter positions in the LASER dataset. Uniformly divided 2000×2000 bins in latitude and longitude are applied to compute the histogram and all snapshots and locations available in the dataset are included. (right) Four regions of interest, to be individually analyzed in section 6c. Each region is of a circular shape in the latitude–longitude space, and the radius of each circle is 0.3° .

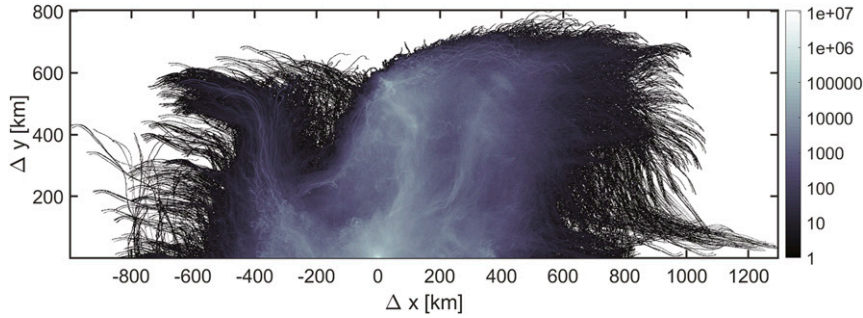


FIG. 9. Histogram of drifter pair separation vectors accumulated from all available observations in the LASER dataset. Uniform 1000×1000 bins in $(\Delta x, \Delta y)$ are applied to compute the histogram.

$$\Delta x = R(\lambda_2 - \lambda_1)\{\cos[(\theta_2 + \theta_1)/2]\}, \quad (50)$$

which was used in Balwada et al. (2016).

As the error in the drifter positions is roughly 10m, we discard all the drifter pairs whose separation distances are smaller than 0.1 m and group all the drifter pairs whose separation distances are between 0.1 and 30 m into a single first bin in r . We have verified that if we, say, only require the separation distances smaller than 10 m to be grouped into the first bin, the diagnosed rotational or divergent structure functions change little at scales larger than 100 m. To make the statistical error more uniform across scales, we set the bin widths at separation distances larger than 30 m such that the numbers of drifter pairs is similar in each bin. As a result, the bin centers of r are not guaranteed to be equally spaced.

b. Global statistics

We first apply our algorithm to all the available observations in LASER, as depicted in Fig. 8. This is a brute force test of the robustness of our method, as it is unlikely that this large-scale dataset will be well described by homogeneous or stationary statistics. In Fig. 9 we plot a histogram of separation vectors to get a sense on how anisotropic the distribution is. The distribution of separation vectors is not generally isotropic, and at $r > 400$ km, there are significant gaps in angles in the

histogram. Hence we discard all drifter pairs with $r > 300$ km. We apply 1000 bins for $r > 30$ m, in each of which there are some 592 000 drifter pairs. Increasing or decreasing the number of bins by a factor of 4 did not significantly change the results. The $n \in \{0, 2, 4\}$ modes of D_{LL} , D_{TT} , and D_{LT} estimated from data are plotted in Fig. 10. At $r \rightarrow 300$ km, not all the modes are consistent with the decorrelation limits derived in (36) and (37). Hence, it is likely that the data are not decorrelated there. We note that this would not affect the Helmholtz decomposition of structure functions: observing formulas (41), the data at larger separation distances do not affect the outcomes. Nevertheless, if one further conducts a spectra analysis based on structure functions, which involves Fourier transforms that require information at all r in the computations of spectral quantities (i.e., power spectra), this should be kept as a caveat.

From Fig. 10, at distances smaller than 100 km, the isotropic modes $D_{LL}^{e0}(r)$ and $D_{TT}^{e0}(r)$ are stronger than the anisotropic modes. Hence, unless there are significant cancellations in the Helmholtz decomposition formulas (41), the same should be true for the Helmholtz modes at these distances. Moreover, as the underlying functions are nearly isotropic at these distances, the angle weighting is not expected to make a difference at distances smaller than 100 km. These turn out to be the case, as reflected in the Helmholtz decomposition outcomes presented in separate modes, plotted in Fig. 11. The angle weighting does

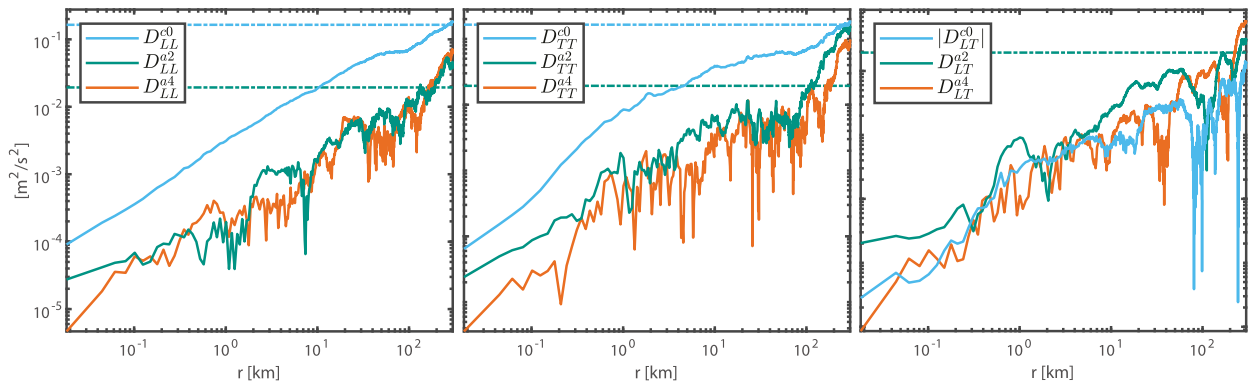


FIG. 10. The $n = 0, n = 2$, and $n = 4$ modes of (left) D_{LL} , (center) D_{TT} , and (right) D_{LT} from all data available in LASER, estimated from the angle-weighted approach. The dash-dot lines mark the estimated decorrelation limits as $r \rightarrow \infty$, from (36) and (37). As in the synthetic examples, for anisotropic modes, the absolute value of the modes defined in (11) are presented for convenience. Note that from now on we will present figures in logarithmic scales, which was not the case in the synthetic experiment.

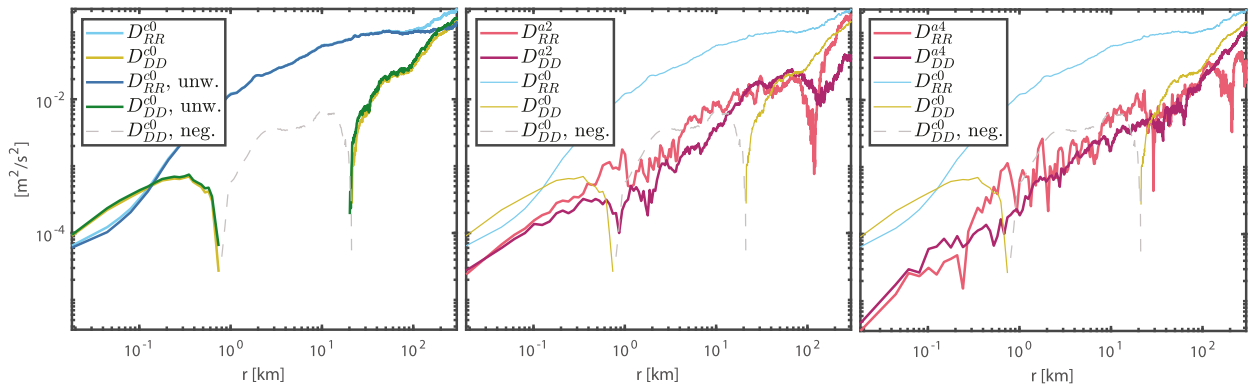


FIG. 11. Helmholtz decomposition of second-order structure functions at (left) $n = 0$, (center) $n = 2$, and (right) $n = 4$ modes from all data available in LASER. Line legends and colors are as in Fig. 7, but that the gray lines now denote nonphysically negative components of $D_{DD}^{c0}(r)$ diagnosed from the angle-weighted approach, as marked by “neg” in the line legends. The $n = 0$ modes diagnosed from the angle-weighted approach are reproduced in the middle and right panels for convenience in the comparison of the magnitudes between the $n = 0$ modes and the anisotropic modes.

make a difference in the Helmholtz decomposition outcome (Fig. 11, first panel) at distances larger than 100 km, where the anisotropic components in the underlying velocity structure functions are strong (Fig. 10). At these large distances, the unweighted results give a near equipartation between rotational and divergent components, while the angle-weighted results still present a larger rotational component over the divergent component at the zeroth mode.

The outcomes could be confusing in their physical implications. For example, at the largest separation distances $r > 100$ km, even though $D_{RR}^{c0}(r)$ is consistently larger than $D_{DD}^{c0}(r)$, they differ by just about a factor of 2. Meanwhile, the anisotropic component in $D_{RR}(r, \alpha)$ is about as strong as $D_{RR}^{c0}(r)$ (Fig. 11, second panel) there. If we add the zeroth mode and the two anisotropic modes together, reconstruct $D_{RR}(r, \alpha)$ and $D_{DD}(r, \alpha)$ in 2D by the truncated Fourier series (7), it would turn out that at certain angles, $D_{RR}(r, \alpha)$ is sometimes weaker than $D_{DD}(r, \alpha)$ at distances larger than 100 km. It seems likely that this is not a physical effect, but to do with error or violations of our assumptions, such as the inhomogeneity of the data at such large separation distances.

c. Statistics in different subregions

We now apply the Helmholtz decomposition on data spatially confined in four different smaller regions marked in Fig. 8, each of which spans 0.3° in latitude and longitude. We select the four regions roughly based on the spatial density of available observations, picking the four most densely observed regions. Among those that entered the regions, on average, drifters stayed for about 137 h in region 1, 238 h in region 2, 55 h in region 3, and 174 h in region 4. The regions 1 and 2, which appear as strong convergence zones, are close to the deployment locations of 840 drifters, some of which got caught into a mesoscale oceanic front (Nouguier et al. 2018) and passed region 3. About 150 drifters were then further advected into region 4, while the remaining joined the surrounding eddies.

Our motivations to study the smaller spatial regions is mainly concerned with inhomogeneities in data. Most drifters

in the LASER operation are deployed in a conscious effort to focus on frontal areas (Novelli et al. 2017, p. 20), and the drifters that sketch the surrounding mesoscale features are rather sparsely distributed in comparison. As reflected the histogram of drifter positions shown in Fig. 8, there is a clear concentration of observations in a relatively narrow spatial range (D’Asaro et al. 2018; Pearson et al. 2019). Including the very sparsely observed regions could then introduce statistical error at larger separation distances. Moreover, the underlying dynamics does not appear homogeneous across the range covered in the LASER operation. Due to the rich variety of dynamics sampled, if we average over all data covered in LASER, it becomes less clear what does the location-smear quantities mean physically. Especially, as we do not weight observations based on deployment locations or surrounding dynamical conditions, spatial areas that are densely observed are likely the main contributors to the averaged statistics. We will find out that this is indeed the case: the outcomes from region 2 will appear similar to outcomes from the “global statistics.” By inspecting smaller regions, within each of which the area is more uniformly sampled and the underlying dynamics are less qualitatively different, we could hopefully get location-smear quantities that are more meaningful physically.

In Fig. 12, we present the histograms of separation vectors in the four regions. In the calculations of structure functions, we will cut off at $r = 30$ km for all the four regions, which are marked by the dashed half-circles in Fig. 12. Beyond this radius, the outcomes in region 3 and 4 would suffer significantly from statistical error due to the gaps in separation angles. We have checked that the velocity structure function modes do not approach the decorrelation limits derived in (36) and (37), which is not surprising at such a small cutoff distance. The binning in r in the four regions is detailed as follows. Between $r = 30$ m and $r = 30$ km, in region 1, there are 1000 bins, each of which contains about 26 000 drifter pairs; in region 2, there are 244 bins, each of which contains 200 000 drifter pairs; in region 3, there are 248 bins, each of which contains 6500 drifter pairs; and in region 4, there are 999 bins, each of which contains 3800 pairs.

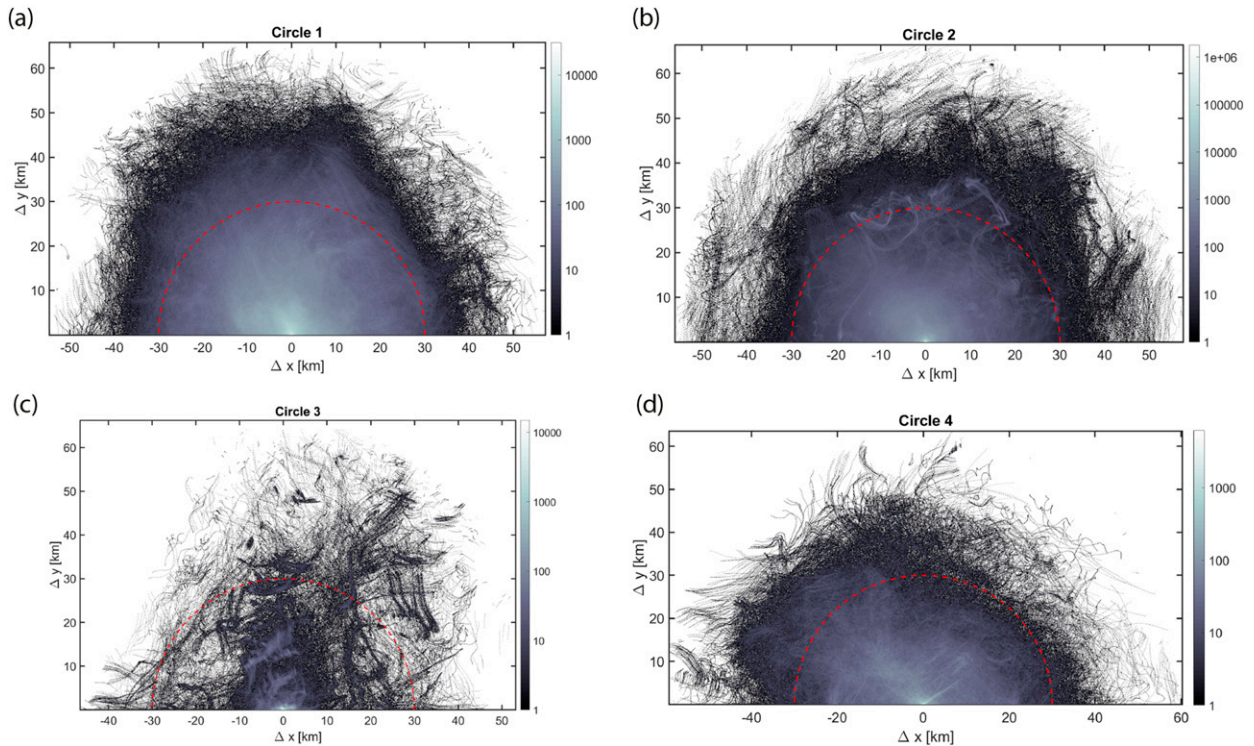


FIG. 12. (a)–(d) Histograms of separation vectors of drifter pairs at different spatial subregions in the LASER dataset for regions 1, 2, 3, and 4, respectively. All snapshots are included. The dashed half-circles mark the radius at $r = 30$ km.

The numbers of bins in the four regions are set differently in such an odd way mainly because we want the first bins to be all centered around 20 m for conveniences in presentations. The results would not contain significant differences at scales larger than 100 m if we vary the number of bins by a factor of 4 in each region.

The Helmholtz decomposition now delivers strikingly different outcomes in the four different regions, as depicted in detail for the Fourier modes in Fig. 13. To more straightforwardly present which component is dominating, we sum the Fourier modes and display the ratio $D_{RR}/(D_{RR} + D_{DD})$ for the four regions in Fig. 14.

The ratio appears strongly anisotropic in region 1 across all distances covered, showing that either the rotational or the divergent component could dominate at different angles. In region 2, we refrain from making interpretations due to the nonphysically negative values diagnosed. As to be discussed in detail in section 6d, these negative values in region 2 might not be merely a negligible numerical artifact. In region 3, at any distances, there does not seem to be a strong tendency for either the rotational or divergent component to dominate. The ratio revealed in region 4 shows a dominance of rotational component at larger distances, and a mixture of near-equipartition and dominance of divergent component at smaller distances. The transition distance in region 4 is at around 1 km.

These outcomes are interesting in several aspects. First, the dynamics are qualitatively different between region 1 and region 2, even though they seem to be both convergent regions spatially close to each other. Second, at $r < 30$ km, the

Helmholtz decomposition from region 2 is quite similar to those from the global statistics (comparing Fig. 11 and Fig. 13, second row). This is understandable, as region 2 is more densely sampled than other regions (as reflected in the histogram Fig. 8), and the collective statistics would strongly favor the more densely sampled regions. When one calculates a simple ensemble average of the global statistics as in section 6b, one may well be tempted into thinking that the outcome somewhat reflects the tendency of the general dynamics in the whole region, while in fact, the outcomes are dominantly contributed by just region 2 only. This echoes with the rising concerns on the bias caused by the uneven sampling of Lagrangian statistics (D'Asaro et al. 2018; Pearson et al. 2019, 2020).

Third, anisotropy in the diagnosed $D_{RR}(r, \alpha)$ and $D_{DD}(r, \alpha)$ is strong in region 3 at separation distances as small as 1 km, which is perhaps surprising, as isotropy is usually assumed to hold at such small scales. Fourth, in regions 1 and 3, the rotational components do not show a tendency to dominate toward larger distances. We note that this is not in direct contradiction with the belief that mesoscale eddies are dominated by rotational flows: the largest distance covered here is 30 km, so the rotational motion could still be dominating at mesoscales, and we just cannot resolve that here. Nevertheless, what leads to the strong presence of divergent motion at distances up to 30 km in these regions is intriguing.

Finally, the angle weighting makes a modest difference in the zeroth modes of the rotational or divergent structure functions in these four regions. The explanation to this goes back to the previous observation in section 3 that the angle

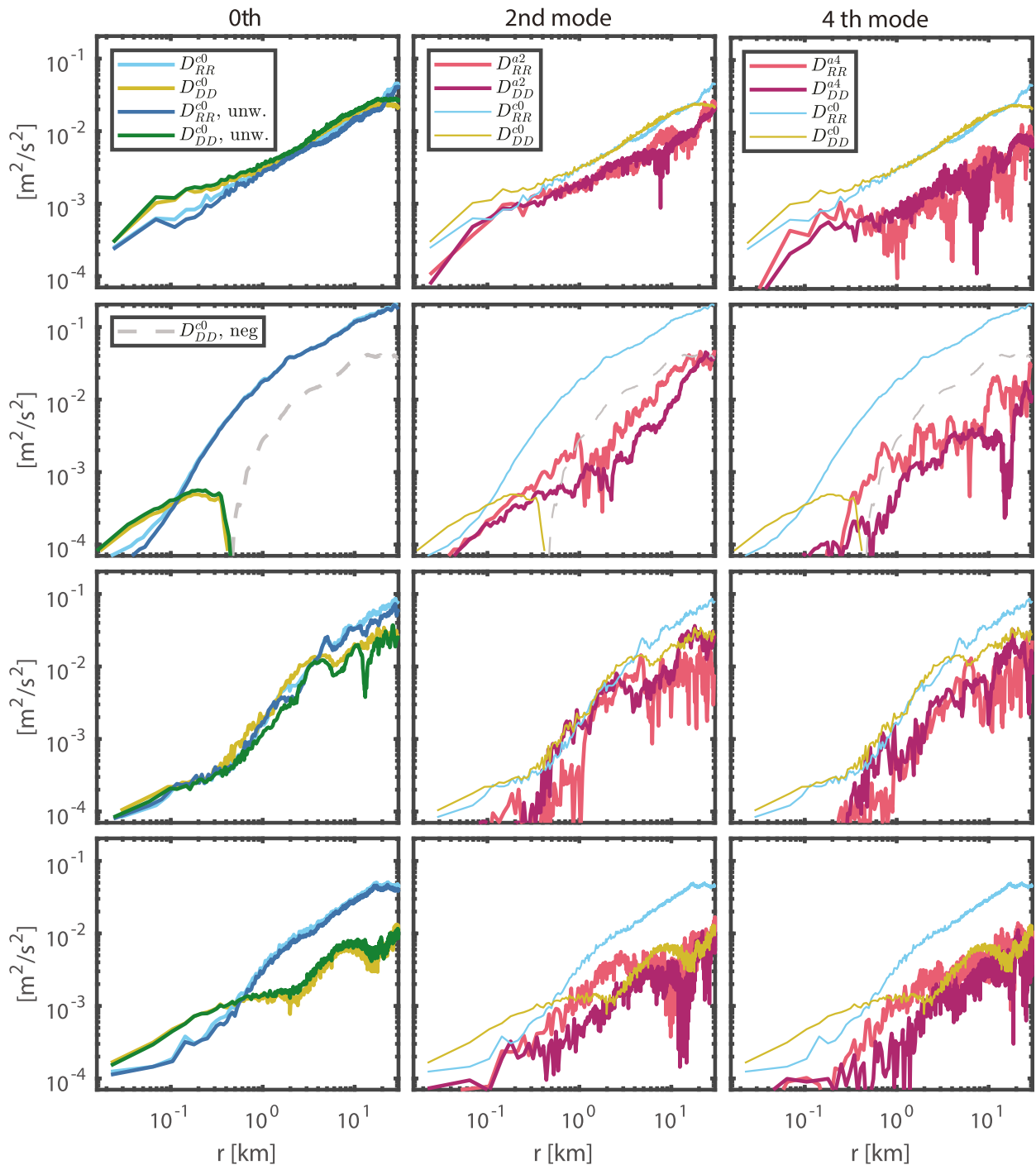


FIG. 13. Helmholtz decomposition for the four subregions. Four rows correspond to the four different subregions in order. The legends and line specifications are as in Fig. 11. Magnitudes smaller than $7 \times 10^{-5} \text{ m}^2 \text{ s}^{-2}$ are omitted in the plots.

weighting could make a difference only when both the distribution of separation vectors and the underlying functions are anisotropic. The only region that appears to possess strong anisotropy in both the distribution and the functions $D_{RR}(r, \alpha)$ and $D_{DD}(r, \alpha)$ is region 3. In region 3, although the visual difference between the weighted and unweighted outcomes is

small in Fig. 13 (third row), they actually differ by about a factor of 2 at some distances, which is significant quantitatively.

d. Nonphysical negative values

One initial motivation to this work was to investigate if incorporating anisotropy could mitigate the nonphysically

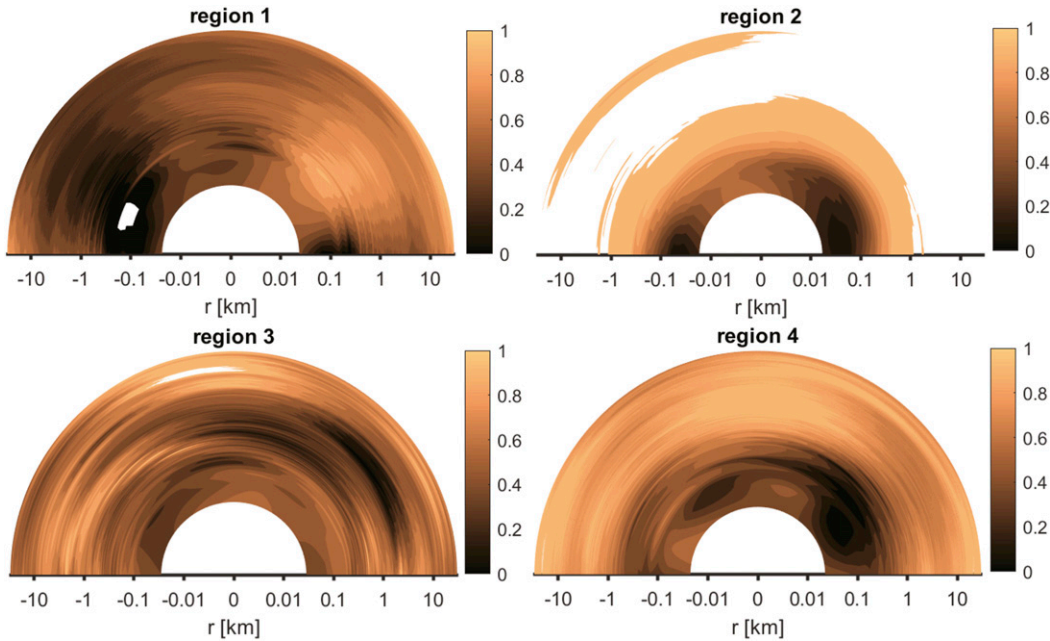


FIG. 14. The ratio $D_{RR}/(D_{RR} + D_{DD})$ calculated from observations that fall in regions 1, 2, 3, and 4, respectively. Regions where D_{DD} or D_{RR} are diagnosed negative are left blank. Note the logarithmic scale in r .

negative values that sometimes occur when isotropy is assumed (Lindborg 2015). In our framework, following the respective definitions, any negative values diagnosed in the 2D functions $D_{RR}(r, \alpha)$ or $D_{DD}(r, \alpha)$ should be nonphysical, and so are any negative values in the zeroth modes $D_{RR}^0(r)$ or $D_{DD}^0(r)$.

We find in our analysis of LASER data that even with angle weighting, such nonphysical values still sometimes occur. At the zeroth modes, there turns out to be negative components in D_{DD}^0 in the global statistics and the outcomes from region 2 (Fig. 11 and Fig. 13, second row). In the estimated 2D functions, negative values of $D_{DD}(r, \alpha)$ appear quite pronounced in region 2, corresponding to the blank patches in the second panel of Fig. 14. In region 1 and 3, there are occasional negative values in either $D_{DD}(r, \alpha)$ or $D_{RR}(r, \alpha)$, which correspond to the smaller blank fragments marked in Fig. 14.

Such nonphysical values can be attributed to violations of our assumptions [i.e., homogeneity, stationarity, and isotropy of $C_{\psi\phi}(r, \alpha)$], or error in our estimations. The error in our estimations can arise from statistical noise and numerical integration error. Moreover, in the estimations of the 2D functions, there might also be significant truncation error as we only include the modes at $n = 0, 2, 4$ in the azimuthal Fourier series. Even if a 2D function $f(r, \alpha)$ is nonnegative everywhere, its truncated azimuthal Fourier series is not guaranteed to be nonnegative. For example, $f(r_0, \alpha) = \exp[-4 \cos(\alpha)^2]$ is nonnegative, but its Fourier series truncated at $n = 2$ is not. As noted before, we cannot include arbitrarily high modes in the series, as the higher modes would be more sensitive to statistical noise. Theoretically, one may be able to find an optimal cutoff number that balances the statistical noise and the truncation error. We consider the pursuit of this to be beyond the scope of this project.

In terms of *relative error*, the negative values diagnosed in the LASER data are mild in most instances. At the zeroth modes, when the negative $D_{DD}^0(r)$ are diagnosed in the global statistics and in region 2 (Fig. 11 and Fig. 13, second row), the magnitude of $D_{RR}^0(r)$ are indeed consistently greater (at least 5 times larger) than $D_{DD}^0(r)$ in our results. This means that the relative error in $D_{RR}^0(r)$ should be less than 20%. When such negative values are noted in previous analysis on atmospheric track data (Lindborg 2015) or model outputs (Bierdel et al. 2016), the situation appears similar.

For the 2D functions, in region 2, we compute the ratio $|D_{RR}(r, \alpha)/D_{DD}(r, \alpha)|$ when $D_{DD}(r, \alpha)$ is diagnosed negative. This ratio corresponds to whether or not $D_{RR}(r, \alpha)$ is much larger than $[-D_{DD}(r, \alpha)]$ when D_{DD} is nonphysical. In region 2, we find out that sometimes $D_{RR}(r, \alpha)$ is about just 2 or 3 times as large as $[-D_{DD}(r, \alpha)]$, which means that the negative values diagnosed could constitute a significant relative error in $D_{RR}(r, \alpha)$, at least in the infinity norm. Hence, we should be cautious on the validity of our results in region 2.

Fortunately, in region 1 and 3, whenever a negative component is diagnosed, the positive component is always at least 5 times larger than the magnitude of the negative component. We have checked this is also the case in the global statistics. Overall, when a negative component is diagnosed in 2D, the relative error in the positive component appears to be strong only in region 2.

7. Discussions and summary

Our new algorithm reported here consisted of two parts. First, we pointed out a potential source of systematic error from the unweighted ensemble averaging that is traditionally

applied in the evaluations of structure functions and proposed an angle-weighted approach instead, which takes account of the anisotropic distribution of separation vectors (section 3). The angle-weighted approach, as well as the analysis of 2D functions through the lens of azimuthal Fourier expansions to include anisotropy, can be applied on the estimations of other spatially dependent scalar-based quantities, such as higher-order structure functions and relative dispersions too.

Second, a set of Helmholtz decomposition formulas (41), which diagnoses the azimuthal Fourier modes separately in a systematic manner, was derived for sparse 2D data. The conditions for this set of formulae to work are stationarity, homogeneity, and that the correlation $C_{\psi\psi}(r, \alpha)$ is either zero or a function of r only (but see section 4e for an extension to odd Fourier modes). No further assumptions or constraints were called upon, and the required observations for the decomposition are the same as the ones for the isotropic Helmholtz decomposition algorithm (Lindborg 2015). The algorithm was verified using synthetic examples (section 5) and applied for the LASER observational dataset (section 6).

In the applications to the LASER data, we first compute the statistics from all snapshots and locations, and then from four different smaller spatial regions separately. The strength of anisotropic modes, as well as the ratio between the rotational and divergent structure functions, turn out quite diverse across the four different subregions, suggesting different dynamics underlying them. We also find along the way that the statistics from region 2 only appear similar to the statistics from all areas available in the LASER data, which illustrates that averaging over a region that is sampled highly nonuniformly can be problematic.

Whenever possible we have checked the robustness of our method by varying details such as bin sizes and averaging algorithms. However, there are still some potentially significant issues we have not addressed. For the theory we had to assume that $S_{\psi\psi}(r, \alpha)$ is either zero or isotropic, the violation of which could make the Helmholtz decomposition formulas (41) invalid at anisotropic modes. We have not investigated if stationarity holds in data. Similar to homogeneity, stationarity may also be considered as an operation that smears out time dependency, rather than an assumption about the dynamics, and some small variations in time would not blur the physical meaning of the averaged outcomes. However, this could be questioned in the LASER data, due to for example some high wind events that took place during the operation (Lodise et al. 2019). The CARTHE drifters in LASER are drogued close to surface at 0.5 m, and we have not studied the impacts of direct wind forcing yet.

Some minor issues are as follows. The LASER data product we use could itself contain some space for improvements (Haza et al. 2018). The subregions in the analysis in LASER as in section 6 are handpicked roughly based on the density of observations, and the shapes of these subregions are chosen to be round in latitude–longitude space for convenience. Other more sophisticated clustering approaches (D’Asaro et al. 2018) may help pick the subregions in a more systematic manner with better results.

As a direct comparison with previous work assuming isotropy (Balwada et al. 2016), we have also applied our algorithm

to surface drifter observations from the Grand Lagrangian Deployment campaign in a similar fashion as section 6b. We find that in the global statistics, the anisotropic components in D_{RR} , D_{DD} turn out weak compared to the isotropic components, and accordingly the angle weighting does not make a significant difference. Hence, the observations in (Balwada et al. 2016) stand tested under anisotropy. We include a more detailed report on this in the supplemental material.

While the kinematic Helmholtz decomposition is indicative of the robustness of geostrophic balance, a further dynamical wave–vortex decomposition that can tell different dynamic components apart is certainly more desirable (BCF14). Due to lack of potential energy measurements (such as buoyancy) in the LASER drifter observations, we are currently unable to conduct this further step exactly. If structure functions of buoyancy, or other indicators of potential energy are available, a generalization of the BCF14 linear wave–vortex decomposition algorithm, or more ambitiously, the inclusion of a nonlinear quasigeostrophic correction in the decomposition (Wang and Bühler 2020), should be possible. Such measurement of potential energy either calls on technological advancements of Lagrangian instruments, or a proper synergy of Lagrangian observations with remote sensing data or model simulations. The latter may be particularly interesting, in the prospect of the soon-to-be launched, submesoscale-resolving satellite mission SWOT (Morrow et al. 2019). In principle, one could also make additional assumptions about the relations between different components, such as a Garrett–Munk frequency spectra for the wave energy (BCF14; Cao et al. 2019), and make a wave–vortex decomposition based on that.

Drifter observations are usually well resolved in time; the LASER data product we are applying in this work has a resolution of 15 min. It is intriguing to consider how to combine the spatial information with temporal information. For mooring data, a frequency-resolved structure function has been developed (Callies et al. 2020), but its definition cannot be directly generalized to Lagrangian observations, as Lagrangian recording devices are constantly changing their relative positions. One other approach we have contemplated over is to filter out the higher frequencies, and conduct the Helmholtz again to see if the remaining motion becomes more rotational. A similar idea was investigated in (Beron-Vera and LaCasce 2016), where structure functions were found to be different after inertial oscillations are filtered out. A complication with this approach is that after velocity observations are filtered, the trajectories need to be reintegrated for consistency, and how to determine what are the “new” subregions seems to be a non-trivial question. This is still under exploration.

Acknowledgments. Financial support under Grant DMS-1813891 of the U.S. National Science Foundation and Grant N00014-19-1-2407 of the U.S. Office of Naval Research is gratefully acknowledged. Detailed advice and discussions regarding Lagrangian data treatments from Dhruv Balwada, Joseph Lacase, Jeanna Pearson, Baylor Fox-Kemper, and Helga Huntley are greatly appreciated. Bernard Delyon and François Portier have answered HW’s questions about a KDE-based integral approximation method. We thank William

Young for sharing his notes on spirality with us, which helped clarify the issues in [section 4c](#).

Data availability statement. Codes related to the progress in this study are available at <https://github.com/hannnwang/Anisotropic-Helmholtz-decomposition-for-Lagrangian-data>. The LASER data product (D’Asaro et al. 2017) applied in this work can be openly accessed from <https://gulfresearchinitiative.org>. [Figure 8](#) is plotted applying the MATLAB package (Pawlowicz 2020).

APPENDIX A

Evaluating Azimuthal Fourier Modes

We seek to optimize the numerical approximation of polar integrals such as

$$D_{LL}^{cn}(r) = F_n \int_{-\pi}^{\pi} D_{LL}(r, \alpha) \cos(n\alpha) d\alpha \tag{A1}$$

when the data are given on a regular Cartesian grid. For example, if $n = 0$, we have

$$D_{LL}^{c0}(r) = F_0 \int_{-\pi}^{\pi} \frac{1}{L^2} \sum_{k,l} \hat{D}_{LL}(k, l) e^{i(kx+ly)} d\alpha \tag{A2}$$

$$= F_0 \frac{1}{L^2} \sum_{k,l} \hat{D}_{LL}(k, l) \int_{-\pi}^{\pi} e^{i[kr\cos(\alpha)+lr\sin(\alpha)]} d\alpha, \tag{A3}$$

where the variables (x, y) correspond to (r, α) via the polar-to-Cartesian coordinate transform, and $\hat{D}_{LL}(k, l)$ are the Fourier coefficients of $D_{LL}(x, y)$. The integral is

$$\int_{-\pi}^{\pi} e^{i[kr\cos(\alpha)+lr\sin(\alpha)]} d\alpha = 2\pi J_0(Kr). \tag{A4}$$

If $n = 2$, the evaluation of $D_{LL}^{c2}(r)$ similarly involves the integral

$$\int_{-\pi}^{\pi} \cos(2\alpha) e^{i[kr\cos(\alpha)+lr\sin(\alpha)]} d\alpha. \tag{A5}$$

This can be transformed as

$$\begin{aligned} & \int_{-\pi}^{\pi} \cos(2\alpha) \exp\left\{iKr \cos\left[\frac{\pi}{2} - \arctan\left(\frac{k}{l}\right) - \alpha\right]\right\} d\alpha \\ &= \int_{\frac{\pi}{2} - \arctan\left(\frac{k}{l}\right)}^{\frac{3\pi}{2} - \arctan\left(\frac{k}{l}\right)} -\cos\left[2\arctan\left(\frac{k}{l}\right) + 2\tau\right] e^{iKr\cos\tau} d\tau \\ &= -\cos\left[2\arctan\left(\frac{k}{l}\right)\right] \int_{-\pi}^{\pi} \cos(2\tau) e^{iKr\cos(\tau)} d\tau + \sin\left[2\arctan\left(\frac{k}{l}\right)\right] \int_{-\pi}^{\pi} \sin(2\tau) e^{iKr\cos(\tau)} d\tau \\ &= -\cos\left[2\arctan\left(\frac{k}{l}\right)\right] \int_{-\pi}^{\pi} \cos(2\tau) e^{iKr\cos(\tau)} d\tau \\ &= +\cos\left[2\arctan\left(\frac{k}{l}\right)\right] 2\pi J_2(Kr). \end{aligned} \tag{A6}$$

The integral (A5), and hence $D_{LL}^{c2}(r)$, are then readily evaluated on a regular grid. Similar identities

useful for the evaluation of other $n = 2$ and $n = 4$ terms are

$$\begin{aligned} & \int_{-\pi}^{\pi} \sin(2\alpha) e^{i[kr\cos(\alpha)+lr\sin(\alpha)]} d\alpha \\ &= -2\pi \sin\left[2\arctan\left(\frac{k}{l}\right)\right] J_2(Kr); \\ & \int_{-\pi}^{\pi} \cos(4\alpha) e^{i[kr\cos(\alpha)+lr\sin(\alpha)]} d\alpha \\ &= \frac{2\pi}{K^3 r^3} \cos\left[4\arctan\left(\frac{k}{l}\right)\right] [Kr(-24 + K^2 r^2) J_0(Kr) - 8(-6 + K^2 r^2) J_1(Kr)]; \\ & \int_{-\pi}^{\pi} \sin(4\alpha) e^{i[kr\cos(\alpha)+lr\sin(\alpha)]} d\alpha \\ &= -\frac{2\pi}{K^3 r^3} \sin\left[4\arctan\left(\frac{k}{l}\right)\right] [Kr(-24 + K^2 r^2) J_0(Kr) - 8(-6 + K^2 r^2) J_1(Kr)]. \end{aligned} \tag{A7}$$

APPENDIX B

Alternative Angle-Weighted Approaches

There can be several other approaches to estimate integrals such as (13) with nonuniformly distributed observations. We will describe one other straightforward approach in detail, which attempts to estimate the underlying functions at equally spaced grids in α so as to preserve the spectral accuracy of trapezoidal integrals.

In this approach, we first divide α into several equally spaced bins. Taking four bins as an example, the first bin $[0, \pi/4]$ is centered at $\pi/8$. We conduct a simple unweighted ensemble average of all the observations at r_i that falls into the first bin, and regard the outcome as our estimate of the underlying function at the bin center $(r_i, \pi/8)$. Similarly, we estimate the underlying function at the other three bin centers. A trapezoidal integration can then be conducted over the four equally spaced bin centers. To illustrate this, we conduct a thought experiment similar to the one in section 3. We suppose that the underlying function $D_{LL}(r_i, \alpha)$ still takes the form

$$D_{LL}(r_i, \alpha) = \sin(2\alpha) + 1, \quad (\text{B1})$$

but for purpose of illustration, we now assume that we have 14 drifter pairs that fall into the bin centered at $r = r_i$. Their separation angles α are $0^\circ, 5^\circ, 10^\circ, 15^\circ, 20^\circ, 25^\circ, 30^\circ, 35^\circ, 40^\circ, 50^\circ, 80^\circ, 130^\circ, 150^\circ,$ and 170° . The observations are still assumed to be free from statistical noise. The unweighted ensemble average of Δu_L^2 that fall into the first bin centered at $\pi/8$ is then:

$$\frac{1}{8}[\sin(2 \times 0^\circ) + \dots + \sin(2 \times 40^\circ)] + 1 = 1.58. \quad (\text{B2})$$

We regard the outcome 1.58 as our estimate of $D_{LL}(r_i, \pi/8)$. Similarly, our estimates of $D_{LL}(r_i, 3\pi/8)$, $D_{LL}(r_i, 5\pi/8)$, and $D_{LL}(r_i, 7\pi/8)$ are 1.66, 0.02, and 0.40, respectively. The zeroth mode (13) can then be estimated using the trapezoidal method on the regular grid:

$$\frac{F_0}{2} \left[(1.58 + 1.66) + (1.66 + 0.02) + (0.02 + 0.40) + (0.40 + 1.58) \times \frac{\pi}{4} \right] = 0.91. \quad (\text{B3})$$

In this approach, as the bin centers are equally spaced, the trapezoidal integration features spectral accuracy (Trefethen and Weideman 2014). If one conducts the traditional unweighted averaging on these observations, the outcome would be 1.31, which is worse.

At higher modes at $n \geq 2$, as the main motivation of this angle-weighting approach is to make the best use of the spectral accuracy of trapezoidal integrations of periodic functions, we propose to evaluate the ensemble average of

$$\Delta u_L^2 \cos(2\gamma), \quad (\text{B4})$$

where γ is the center of the angle bin considered, not the separation angles of each drifter pair recorded. This is another difference between the approach proposed in the main text

in section 3. For example, in the first bin, $\gamma = \pi/8$, and $D_{LL}^c(r_i, \pi/8)$ would be estimated as

$$\cos(2 \times \pi/8) \times 1.58 = 1.12, \quad (\text{B5})$$

where the value 1.58 comes from the ensemble average of the zeroth mode (B2). Similarly, our estimate of $D_{LL}^c(r_i, 3\pi/8)$ at the second bin would be -1.17 , and so on. As γ is a constant within each bin, one would only need to evaluate the ensemble average of Δu_L^2 for each bin once, and time them with $\cos(n\gamma)$, which does not change with regard to observations, to get the estimates of $D_{LL}^c(r_i, \alpha)$ at any n in each bin. The separation angle of each pair is only used to categorize the observations into different angle bins. In case the data size is large, this approach may save significant computational resources.

One could increase the number of bins in α from 4 to, say 32, but in our applications, there is no point going much higher, due to the spectral accuracy of trapezoidal integration, and the practical obstacle that if the bins get too refined, eventually there will be a shortage of observations in individual bins.

We have tested this approach in both our synthetic examples described in section 5 and the analysis of LASER data in section 6 with 32 bins in α , and the diagnosed structure function modes we are interested in are not conspicuously different from the ones diagnosed from the angle-weighted approach described in section 3.

In the applications to realistic data, the observations suffer from statistical error, and theoretically, there could be other better approaches to conduct integration in the presence of noise, which may involve estimating the probability distribution density of α (Delyon and Portier 2016). We consider such finer improvements to be beyond the scope of this work.

REFERENCES

- Balwada, D., J. H. LaCasce, and K. G. Speer, 2016: Scale-dependent distribution of kinetic energy from surface drifters in the Gulf of Mexico. *Geophys. Res. Lett.*, **43**, 10 856–10 863, <https://doi.org/10.1002/2016GL069405>.
- Bartello, P., 1995: Geostrophic adjustment and inverse cascades in rotating stratified turbulence. *J. Atmos. Sci.*, **52**, 4410–4428, [https://doi.org/10.1175/1520-0469\(1995\)052<4410:GAAICI>2.0.CO;2](https://doi.org/10.1175/1520-0469(1995)052<4410:GAAICI>2.0.CO;2).
- Bennett, A., and Coauthors, 2006: *Lagrangian Fluid Dynamics*. Cambridge University Press, 310 pp.
- Beron-Vera, F. J., and J. LaCasce, 2016: Statistics of simulated and observed pair separations in the Gulf of Mexico. *J. Phys. Oceanogr.*, **46**, 2183–2199, <https://doi.org/10.1175/JPO-D-15-0127.1>.
- Bierdel, L., C. Snyder, S.-H. Park, and W. C. Skamarock, 2016: Accuracy of rotational and divergent kinetic energy spectra diagnosed from flight-track winds. *J. Atmos. Sci.*, **73**, 3273–3286, <https://doi.org/10.1175/JAS-D-16-0040.1>.
- Bühler, O., J. Callies, and R. Ferrari, 2014: Wave–vortex decomposition of one-dimensional ship-track data. *J. Fluid Mech.*, **756**, 1007–1026, <https://doi.org/10.1017/jfm.2014.488>.
- , M. Kuang, and E. G. Tabak, 2017: Anisotropic Helmholtz and wave–vortex decomposition of one-dimensional spectra. *J. Fluid Mech.*, **815**, 361–387, <https://doi.org/10.1017/jfm.2017.57>.
- Callies, J., R. Ferrari, and O. Bühler, 2014: Transition from geostrophic turbulence to inertia–gravity waves in the atmospheric energy spectrum. *Proc. Natl. Acad. Sci. USA*, **111**, 17 033–17 038, <https://doi.org/10.1073/pnas.1410772111>.

- , O. Bühler, and R. Ferrari, 2016: The dynamics of mesoscale winds in the upper troposphere and lower stratosphere. *J. Atmos. Sci.*, **73**, 4853–4872, <https://doi.org/10.1175/JAS-D-16-0108.1>.
- , R. Barkan, and A. N. Garabato, 2020: Time scales of sub-mesoscale flow inferred from a mooring array. *J. Phys. Oceanogr.*, **50**, 1065–1086, <https://doi.org/10.1175/JPO-D-19-0254.1>.
- Cao, H., Z. Jing, B. Fox-Kemper, T. Yan, and Y. Qi, 2019: Scale transition from geostrophic motions to internal waves in the northern South China Sea. *J. Geophys. Res. Oceans*, **124**, 9364–9383, <https://doi.org/10.1029/2019JC015575>.
- D'Asaro, E., C. Guigand, A. Haza, H. Huntley, G. Novelli, T. Özgökmen, and E. Ryan, 2017: Lagrangian submesoscale experiment (LASER) surface drifters, interpolated to 15-minute intervals. Gulf of Mexico Research Initiative Information and Data Cooperative (GRIIDC), accessed 10 January 2020, <https://doi.org/10.7266/N7W0940J>.
- , and Coauthors, 2018: Ocean convergence and the dispersion of flotsam. *Proc. Natl. Acad. Sci. USA*, **115**, 1162–1167, <https://doi.org/10.1073/pnas.1718453115>.
- Davis, R. E., 1991: Lagrangian ocean studies. *Annu. Rev. Fluid Mech.*, **23**, 43–64, <https://doi.org/10.1146/annurev.fl.23.010191.000355>.
- Delyon, B., and F. Portier, 2016: Integral approximation by kernel smoothing. *Bernoulli*, **22**, 2177–2208, <https://doi.org/10.3150/15-BEJ725>.
- Essink, S., V. Hormann, L. R. Centurioni, and A. Mahadevan, 2019: Can we detect submesoscale motions in drifter pair dispersion? *J. Phys. Oceanogr.*, **49**, 2237–2254, <https://doi.org/10.1175/JPO-D-18-0181.1>.
- Haza, A. C., and Coauthors, 2018: Drogue-loss detection for surface drifters during the Lagrangian Submesoscale Experiment (LASER). *J. Atmos. Oceanic Technol.*, **35**, 705–725, <https://doi.org/10.1175/JTECH-D-17-0143.1>.
- Hoskins, B. J., I. N. James, and G. H. White, 1983: The shape, propagation and mean-flow interaction of large-scale weather systems. *J. Atmos. Sci.*, **40**, 1595–1612, [https://doi.org/10.1175/1520-0469\(1983\)040<1595:TSPAMF>2.0.CO;2](https://doi.org/10.1175/1520-0469(1983)040<1595:TSPAMF>2.0.CO;2).
- LaCasce, J., 2010: Relative displacement probability distribution functions from balloons and drifters. *J. Mar. Res.*, **68**, 433–457, <https://doi.org/10.1357/002224010794657155>.
- , 2016: Estimating eulerian energy spectra from drifters. *Fluids*, **1**, 33, <https://doi.org/10.3390/fluids1040033>.
- Lindborg, E., 1999: Can the atmospheric kinetic energy spectrum be explained by two-dimensional turbulence? *J. Fluid Mech.*, **388**, 259–288, <https://doi.org/10.1017/S0022112099004851>.
- , 2015: A Helmholtz decomposition of structure functions and spectra calculated from aircraft data. *J. Fluid Mech.*, **762**, R4, <https://doi.org/10.1017/jfm.2014.685>.
- Lodise, J., T. Özgökmen, A. Griffa, and M. Berta, 2019: Vertical structure of ocean surface currents under high winds from massive arrays of drifters. *Ocean Sci.*, **15**, 1627–1651, <https://doi.org/10.5194/os-15-1627-2019>.
- Lumpkin, R., T. Özgökmen, and L. Centurioni, 2017: Advances in the application of surface drifters. *Annu. Rev. Mar. Sci.*, **9**, 59–81, <https://doi.org/10.1146/annurev-marine-010816-060641>.
- Morrow, R., and Coauthors, 2019: Global observations of fine-scale ocean surface topography with the Surface Water and Ocean Topography (SWOT) mission. *Front. Mar. Sci.*, **6**, 232, <https://doi.org/10.3389/fmars.2019.00232>.
- Nastrom, G., and K. S. Gage, 1985: A climatology of atmospheric wavenumber spectra of wind and temperature observed by commercial aircraft. *J. Atmos. Sci.*, **42**, 950–960, [https://doi.org/10.1175/1520-0469\(1985\)042<0950:ACOWS>2.0.CO;2](https://doi.org/10.1175/1520-0469(1985)042<0950:ACOWS>2.0.CO;2).
- Nouguier, F., B. Chapron, F. Collard, A. A. Mouche, N. Rasche, F. Ardhuin, and X. Wu, 2018: Sea surface kinematics from near-nadir radar measurements. *IEEE Trans. Geosci. Remote Sens.*, **56**, 6169–6179, <https://doi.org/10.1109/TGRS.2018.2833200>.
- Novelli, G., C. M. Guigand, C. Cousin, E. H. Ryan, N. J. Laxague, H. Dai, B. K. Haus, and T. M. Özgökmen, 2017: A biodegradable surface drifter for ocean sampling on a massive scale. *J. Atmos. Oceanic Technol.*, **34**, 2509–2532, <https://doi.org/10.1175/JTECH-D-17-0055.1>.
- Özgökmen, T., 2015: Glad experiment code-style drifter trajectories (low-pass filtered, 15 minute interval records), northern Gulf of Mexico near Desoto Canyon, July–October 2012. Gulf of Mexico Research Initiative, accessed 5 October 2019, <https://doi.org/10.7266/N7VD6WC8>.
- Pawlowicz, R., 2020: M_map: A mapping package for Matlab, version 1.4.m. <https://www.eoas.ubc.ca/~rich/map.html>.
- Pearson, J., B. Fox-Kemper, R. Barkan, J. Choi, A. Bracco, and J. C. McWilliams, 2019: Impacts of convergence on structure functions from surface drifters in the Gulf of Mexico. *J. Phys. Oceanogr.*, **49**, 675–690, <https://doi.org/10.1175/JPO-D-18-0029.1>.
- , and Coauthors, 2020: Biases in structure functions from observations of submesoscale flows. *J. Geophys. Res. Oceans*, **125**, e2019JC015769, <https://doi.org/10.1029/2019JC015769>.
- Poje, A. C., and Coauthors, 2014: Submesoscale dispersion in the vicinity of the Deepwater Horizon spill. *Proc. Natl. Acad. Sci. USA*, **111**, 12 693–12 698, <https://doi.org/10.1073/pnas.1402452111>.
- , T. M. Özgökmen, D. J. Bogucki, and A. Kirwan, 2017: Evidence of a forward energy cascade and Kolmogorov self-similarity in submesoscale ocean surface drifter observations. *Phys. Fluids*, **29**, 020701, <https://doi.org/10.1063/1.4974331>.
- Qiu, B., T. Nakano, S. Chen, and P. Klein, 2017: Submesoscale transition from geostrophic flows to internal waves in the northwestern Pacific upper ocean. *Nat. Commun.*, **8**, 14055, <https://doi.org/10.1038/ncomms14055>.
- Rasmussen, C. E., 2003: Gaussian processes in machine learning. *Summer School on Machine Learning*, Springer, 63–71.
- Richardson, L. F., and H. Stommel, 1948: Note on eddy diffusion in the sea. *J. Meteor.*, **5**, 238–240, [https://doi.org/10.1175/1520-0469\(1948\)005<0238:NOEDIT>2.0.CO;2](https://doi.org/10.1175/1520-0469(1948)005<0238:NOEDIT>2.0.CO;2).
- Stewart, K., P. Spence, S. Waterman, J. Le Sommer, J.-M. Molines, J. Lilly, and M. H. England, 2015: Anisotropy of eddy variability in the global ocean. *Ocean Modell.*, **95**, 53–65, <https://doi.org/10.1016/j.ocemod.2015.09.005>.
- Trefethen, L. N., and J. Weideman, 2014: The exponentially convergent trapezoidal rule. *SIAM Rev.*, **56**, 385–458.
- Waite, M. L., 2020: Untangling waves and vortices in the atmospheric kinetic energy spectra. *J. Fluid Mech.*, **888**, F1, <https://doi.org/10.1017/jfm.2019.1060>.
- Wang, H., and O. Bühler, 2020: Ageostrophic corrections for power spectra and wave-vortex decomposition. *J. Fluid Mech.*, **882**, A16, <https://doi.org/10.1017/jfm.2019.815>.
- Yaglom, A. M., 2004: *An Introduction to the Theory of Stationary Random Functions*. Courier Corporation, 258 pp.
- Zhang, F., J. Wei, M. Zhang, K. Bowman, L. Pan, E. Atlas, and S. Wofsy, 2015: Aircraft measurements of gravity waves in the upper troposphere and lower stratosphere during the start08 field experiment. *Atmos. Chem. Phys.*, **15**, 7667–7684, <https://doi.org/10.5194/acp-15-7667-2015>.
- Zhurbas, V., G. Väli, and N. Kuzmin, 2019: Rotation of floating particles in submesoscale cyclonic and anticyclonic eddies: a model study for the southeastern Baltic Sea. *Ocean Sci.*, **15**, 1691–1705, <https://doi.org/10.5194/os-15-1691-2019>.